# OPEN BIOLOGY

royalsocietypublishing.org/journal/rsob

### Research





**Cite this article:** Ranaivoson FM *et al.* 2023 Nucleotide-free structures of KIF20A illuminate atypical mechanochemistry in this kinesin-6. *Open Biol.* **13**: 230122.

https://doi.org/10.1098/rsob.230122

Received: 28 April 2023 Accepted: 18 August 2023

#### Subject Area:

structural biology/biochemistry/biophysics

#### **Keywords:**

kinesin, KIF20A, motor activity, microtubule assembly, cytokinesis

#### Author for correspondence:

Anne Houdusse

e-mail: anne.houdusse@curie.fr

Electronic supplementary material is available online at https://doi.org/10.6084/m9.figshare. c.6821440.

# THE ROYAL SOCIETY

# Nucleotide-free structures of KIF20A illuminate atypical mechanochemistry in this kinesin-6

Fanomezana Moutse Ranaivoson<sup>1</sup>, Vincent Crozet<sup>1</sup>, Matthieu P. M. H. Benoit<sup>2</sup>, Amna Abdalla Mohammed Khalid<sup>3</sup>, Carlos Kikuti<sup>1</sup>, Helena Sirkia<sup>1</sup>, Ahmed El Marjou<sup>1</sup>, Stéphanie Miserey-Lenkei<sup>1</sup>, Ana B. Asenjo<sup>2</sup>, Hernando Sosa<sup>2</sup>, Christoph F. Schmidt<sup>3,5</sup>, Steven S. Rosenfeld<sup>4</sup> and Anne Houdusse<sup>1</sup>

FMR, 0000-0001-5599-2682; VC, 0000-0002-8864-9415; MPMHB, 0000-0002-2880-7717; CK, 0000-0001-5928-2776; HS, 0000-0001-6849-886X; AEM, 0000-0002-0149-428X; SM-L, 0000-0003-4994-0258; ABA, 0000-0003-3752-9453; HS, 0000-0002-0483-5369; CFS, 0000-0003-2864-6973; SSR, 0000-0003-1909-7116; AH, 0000-0002-8566-0336

KIF20A is a critical kinesin for cell division and a promising anti-cancer drug target. The mechanisms underlying its cellular roles remain elusive. Interestingly, unusual coupling between the nucleotide- and microtubule-binding sites of this kinesin-6 has been reported, but little is known about how its divergent sequence leads to atypical motility properties. We present here the first high-resolution structure of its motor domain that delineates the highly unusual structural features of this motor, including a long L6 insertion that integrates into the core of the motor domain and that drastically affects allostery and ATPase activity. Together with the high-resolution cryo-electron microscopy microtubule-bound KIF20A structure that reveals the microtubule-binding interface, we dissect the peculiarities of the KIF20A sequence that influence its mechanochemistry, leading to low motility compared to other kinesins. Structural and functional insights from the KIF20A pre-power stroke conformation highlight the role of extended insertions in shaping the motor's mechanochemical cycle. Essential for force production and processivity is the length of the neck linker in kinesins. We highlight here the role of the sequence preceding the neck linker in controlling its backward docking and show that a neck linker four times longer than that in kinesin-1 is required for the activity of this motor.

#### 1. Introduction

Cell division requires the collective action of motor proteins in a precisely regulated manner, including several kinesins (Kin) that drive key steps in mitosis [1]. Among these, the Kin-6 KIF20A (MKLP2, Rabkinesin-6) plays critical roles during the metaphase/anaphase transition and cytokinesis [2,3]. KIF20A is a plus end directed motor that was initially identified as a RAB6 effector that promotes dissociation of RAB6-positive vesicles from Golgi membranes by partnering with myosin-2 [4–6]. In mitosis, KIF20A triggers the translocation of the chromosomal passenger complex (CPC) from the centromeres to the spindle midzone and its subsequent enrichment at the equatorial cortex to control furrow ingression and abscission [7,8].

© 2023 The Authors. Published by the Royal Society under the terms of the Creative Commons Attribution License http://creativecommons.org/licenses/by/4.0/, which permits unrestricted use, provided the original author and source are credited.

<sup>&</sup>lt;sup>1</sup>Structural Motility, CNRS UMR144, Institut Curie, Université Paris Sciences et Lettres, Sorbonne Université, 75248 Paris, France

<sup>&</sup>lt;sup>2</sup>Department of Biochemistry, Albert Einstein College of Medicine, Bronx, NY 10461, USA

<sup>&</sup>lt;sup>3</sup>Third Institute of Physics-Biophysics, Georg August University Göttingen, 37077 Göttingen, Germany

<sup>&</sup>lt;sup>4</sup>Department of Pharmacology, Mayo Clinic, Jacksonville, FL 32224, USA

<sup>&</sup>lt;sup>5</sup>Department of Physics and Soft Matter Center, Duke University, Durham, NC 27708, USA

KIF20A is upregulated in a variety of malignancies, and its depletion reduces tumour cell viability [9-13], making it a target and biomarker for cancer therapies. KIF20A is a driver of castration-resistant prostate cancer progression (CRPC) via its role in vesicle secretion and is a promising therapeutic target against CRPC [14]. Paprotrain, the first KIF20A pharmacologic inhibitor discovered [15], induces cytokinetic defects that lead to multi-nucleation. A potent derivative, BKS0349, induces apoptosis and inhibits cell proliferation in a xenograft murine model of endometriosis [16].

KIF20A is regulated by several effectors of the cell cycle including the master mitotic kinases Cdk1/Cyclin-B kinase [17,18], Aurora kinase B [19] and Polo-kinase 1 (Plk1) [20]. Each of the three Kin-6 family members (KIF20A, KIF20B and KIF23) plays distinct roles in cytokinesis [1]. KIF20A and KIF23 guide key mitotic regulators to their proper localization on the spindle midzone and in the midbody, i.e. the CPC (for KIF20A) [7,8] or RacGAP1 (for KIF23) [21,22], while the role of KIF20B is less clear [23].

Despite the importance of KIF20A in mitosis and oncogenesis, little is known about its motor properties and its structure, although this information is critical to define the cellular role of the motor. KIF20A is reported to show minimal transport of low-load or high-load cargo in cells, unlike other mammalian Kin-6 members [24]. How the intriguing, atypical features of its motor domain sequence result in differences in the motor mechanism compared to other previously studied kinesins is currently unknown. KIF20A exhibits unusual kinetic signatures that distinguish it from other motors of the family including a relative uncoupling of the allosteric communication between the nucleotide binding site (NBS) and microtubule interface [25]. Among the kinesin classes, Kin-6 motor domains are unique in having long N- and C-terminal extensions as well as a particular long sequence inserted within loop L6. KIF20A also possesses a neck-linker (NL) four times longer than that of other kinesins (residues 506 to 553).

Previous studies in Kin-1 have shown that elongation of the NL reduces motor processivity [26,27]. Yet KIF20A, despite its elongated NL, has been reported to move processively [28]. Current knowledge about how other kinesin classes allow gating between their heads via restricted positions of their linkers therefore cannot explain how KIF20A functions.

Here we provide a functional characterization of the limits of the motor domain (MD) and the role of both the NL and the unusually long N-terminal extension, thus defining more accurately than in the previous study [25] the length of the physiologically relevant MD that retains all function of KIF20A (FL functional MD, 1-565). We also provide, for the first time, a detailed description of unique sequence differences and their consequences for the structure and function of this atypical kinesin by solving high resolution structures of the nucleotide-free (NF) state of KIF20A, bound and unbound to a microtubule, using cryo-electron microscopy (cryo-EM) and X-ray diffraction, respectively. Detailed insights, previously undescribed with other Kin-6 structures [25,29], concur in providing a framework for understanding the atypical kinetic and motility properties of KIF20A reported here. Another important aspect of this work is that the NL is oriented in the backward direction in the NF state, and we provide a detailed description of how this differs among kinesins. Taken together, this structural and mechanistic study provides the essential framework for deciphering the roles that this unconventional kinesin plays in cells.

## 2. Results

## 2.1. High resolution structures of the nucleotide-free KIF20A motor domain

We obtained a 2.7 Å resolution structure of a microtubuleunbound murine KIF20A fragment (residues 55-510) comprising the MD and the first residues of the NL (figure 1a; electronic supplementary material, figure S1).

This provides the first atomic-resolution model for this atypical kinesin (electronic supplementary material, figure S2, tables S1, S3). Overall, the MD structure displays a typical kinesin fold [31] (figure 1b; electronic supplementary material, figure S1) with the MD in the open conformation, which is generally not observed for isolated kinesins. Instead, this open conformation is one of the conformations observed when kinesins are bound to a microtubule or tubulin [30,32]. Here we chose to apply on KIF20A a subdomain definition based on the recent cryo-EM study of KIF14 [30], as this definition well describes the transition between the conformations observed for the kinesin motor domain along the motor cycle. Several loop insertions unique to KIF20A emerge from the surface of the MD core (figure 1a,c). The most striking ones are in loop L6 (Gly192-Asp295) (figure 1d), which contains a very long insertion of 99 residues when compared to loop L6 of the Kin-1 KIF5B (figure 1a; electronic supplementary material, figure S1). Such a large insertion in L6 is a feature common to all Kin-6 family members.

To assess how microtubule binding influences this KIF20A NF conformation, we also determined the NF structure of the full-length MD, (1-565; figure 2) by cryo-EM, while bound to a microtubule. This construct is extended at both the N- and C-terminus compared to the minimal 55-510 MD construct used for crystallography but it remains monomeric (electronic supplementary material, figure S3). Three-dimensional (3D) classification of the cryo-EM data resulted in two distinct classes (1 and 2) of KIF20A decorating microtubules, with one class (class-1) containing the majority of the particles (66%). Overall resolutions of 3.1 and 3.2 Å were obtained respectively for classes 1 and 2 (electronic supplementary material, figure S4, table S2), with 3.4 and 4.0 Å respectively for the kinesin part. The two classes differ mainly in the orientation of the MD relative to the microtubule so that the minus subdomain in class-2 is positioned further away from the microtubule (figure 2b). Also, the switch loops (L9 and L11) are well resolved in class-1 but not in class-2. Given the further separation from the microtubule interface and the lack of ordering of the switch loops usually associated with microtubule binding in other kinesins [25,30,33], class-2 likely represents a partially unbound intermediate. In both classes the MD is in an open conformation.

The class-1 KIF20A-microtubule complex reveals a net ordering of several structural elements (electronic supplementary material, table S3), including the N-terminal end of helix  $\alpha$ 4 as well as microtubule-binding loops L2 and L12, which are longer in KIF20A than in other kinesins (figure 1a; electronic supplementary material, figure S1, table S3). Therefore, this structure constitutes a net improvement compared to the previous cryo-EM study [25], in which the NF state was reconstructed at much lower resolution (6.1 Å for the kinesin-tubulin complex) and did not allow one to unambiguously trace these elements. Interestingly, upstream to helix  $\alpha 4$ , loop L11 (the switch II

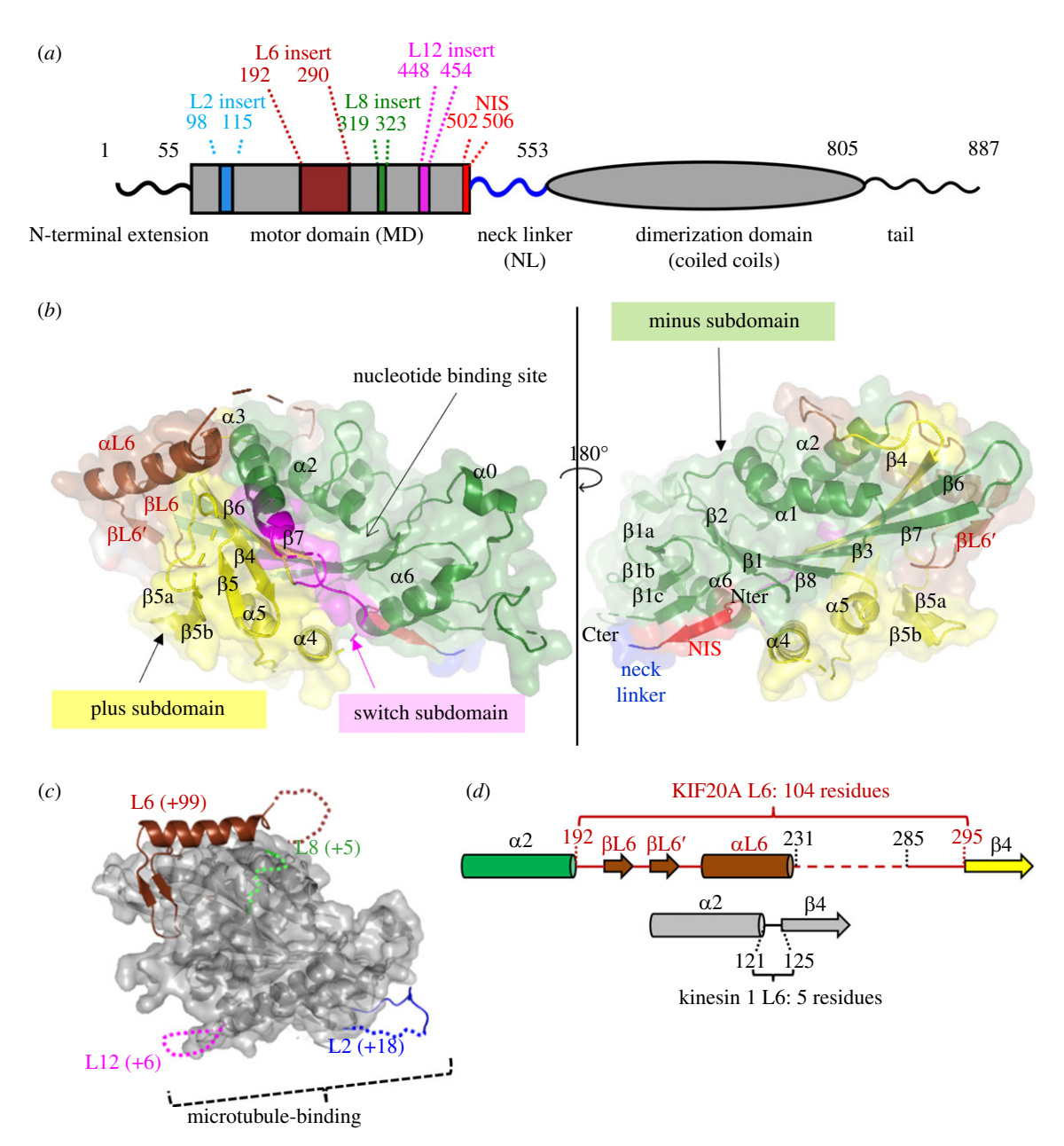


**Figure 1.** Structure of the KIF20A nucleotide-free motor domain. (a) Schematic of the mouse KIF20A highlighting important elements. (b) Crystal structure of the KIF20A MD with its three subdomains as defined in [30], shown in cartoon and semi-transparent surface mode, in two views. The structural elements that belong to the L6 insert ( $\beta$ L6,  $\beta$ L6' and  $\alpha$ L6) are shown in brown. The backward orientation of the 'NL initial segment' (NIS) is highlighted (red). (c) Position and size of the KIF20A loop insertions. For each insertion, the number of KIF20A supplemental residues in comparison with the canonical Kin-1 MD fold is indicated in parentheses. (d) Diagram showing the structural organization of the 104 residue-long KIF20A L6 loop, compared to the 5 residue-long Kin-1 L6 loop.

loop), which is partially disordered in the crystal structure, can be fully traced in the cryo-EM structure, and so can loop L9 (the switch I loop) (figure  $2c_rd$ ). The N-terminally extended  $\alpha 4$ , together with the stabilized L11, serve as a platform for L9 to fold as a  $\beta$ -hairpin, bringing the conserved Arg378 (L9) and Glu412 (L11) to a position where they can form a salt bridge (figure  $2c_rd$ ). It has been established in other kinesins that a salt bridge between the equivalent residues is key for the catalytic hydrolysis of ATP with an important role of the equivalent of Glu412 as a crucial proton acceptor [30,34,35].

#### 2.2. The large specific L6 loop of KIF20A

Loop L6 (Gly192-Asp295) is composed of 104 residues in KIF20A, while in Kin-1 only 5 residues form this loop that links the  $\alpha$ 2b helix and the  $\beta$ 4 strand (figure 3*a*). Rather than extending entirely from the MD, the KIF20A structures show

that this fragment partly folds into it. The N-terminal and C-terminal regions (L6-N, 192–231; L6-C, 286–295) are structured and well defined (electronic supplementary material, figure S2). No density is visible for the central region of L6 (L6-M, Gln232-Pro285) both in crystallographic and cryo-EM density maps (electronic supplementary material, table S3) and its sequence also indicates that it contains flexible or intrinsically disordered regions. The L6-N forms a short  $\beta$ -hairpin and a  $\alpha$ -helix ( $\beta$ L6,  $\beta$ L6' and  $\alpha$ L6) (figures 1b, 3a–c; electronic supplementary material, figure S1) that lies along a surface shared by the plus and minus subdomains (subdomains defined as in [30]). The L6-C region (Asp286-Asp295) adopts an extended conformation between  $\alpha$ 1 and  $\alpha$ 2b (electronic supplementary material, figure S2). This L6-C region is less visible in the cryo-EM map, suggesting it is prone to higher flexibility.

The overall architecture and conformation of L6-N is similar in both X-ray and EM structures as it binds strongly

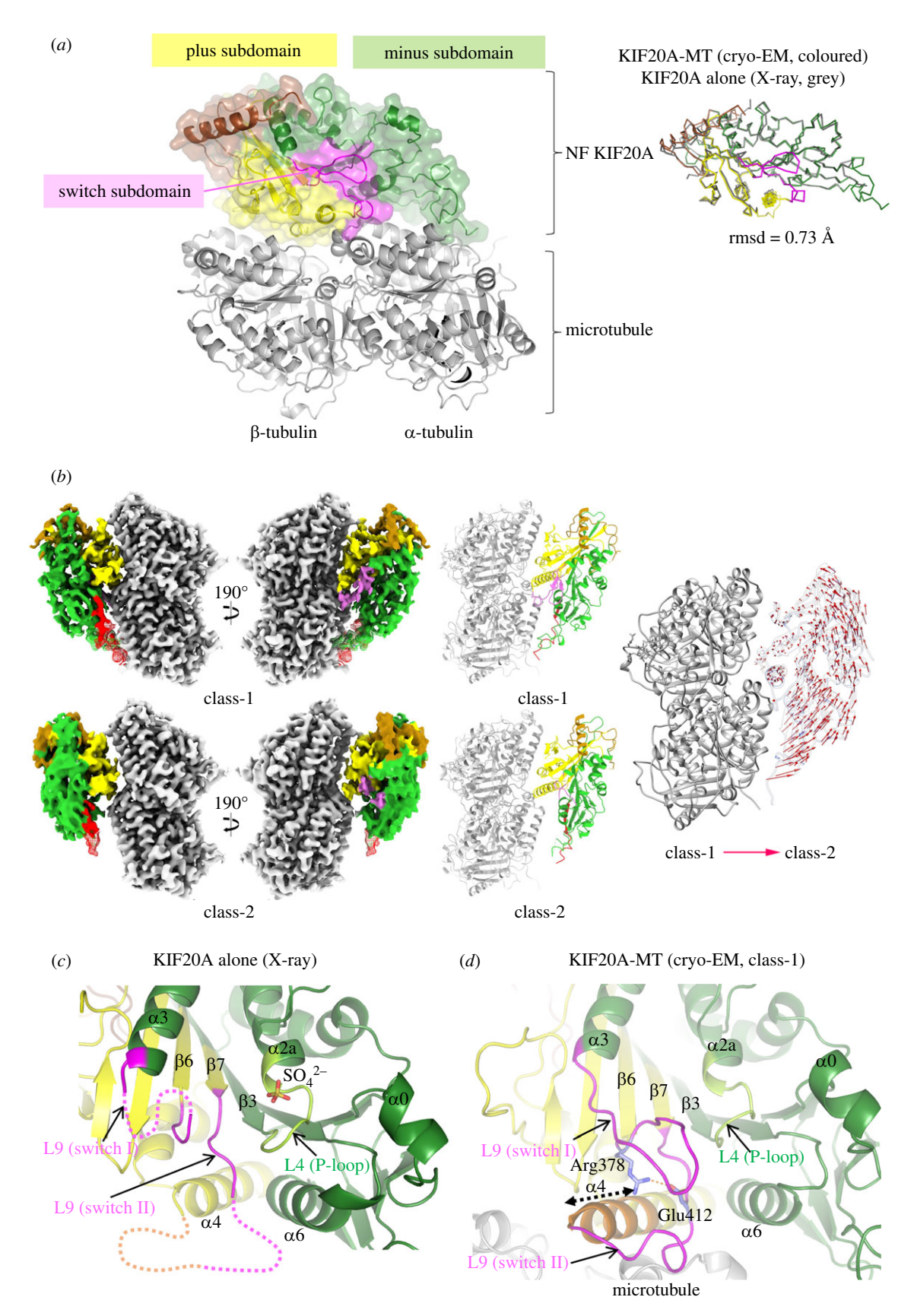


**Figure 2.** Structure of the microtubule-bound KIF20A motor domain and influence of microtubule binding in the structural order of the nucleotide binding site. (a) Overall structure of NF KIF20A-microtubule complex, showing the three kinesin MD subdomains in cartoon and semi-transparent surface mode. The overall KIF20A conformation is similar to that of the MD alone determined by X-ray crystallography (rmsd = 0.73 Å, 286 aligned  $C\alpha$  atoms). (b) Cryo-EM density maps of the two classes of KIF20Amicrotubule complexes rotated 190° from each other (left panel) with corresponding fitted atomic models (centre panel) and a comparison between the two class models (right panel). Regions of the maps and atomic models coloured as in (a). In the right-most panel, the class-1 and class-2 structures are shown superimposed with the red vectors connecting equivalent  $C\alpha$  atoms from the class-1 to the class-2 structure. Note that relative to class-1, the class-2 KIF20A MD is rotated and the areas of the minus subdomain that make contacts with the microtubule in class-1 are further away from the microtubule surface in class-2. (c) The open NBS of KIF20A MD alone (X-ray structure) showing disordered switch loops. Close to the P-loop, a sulfate ion is found at the position normally occupied by the nucleotide βphosphate. (d) The open NBS of KIF20A MD bound to microtubule, showing an ordering of the NBS loops and an extension of the  $\alpha$ 4 helix by three turns upon binding to microtubule. The conserved Arg378 and Glu412 are well positioned for a polar interaction (represented by a red dotted line between  $^{\text{Arg378}}$ N $\eta$ 1 and  $^{\text{Glu412}}$ 0 $\varepsilon$ 2).

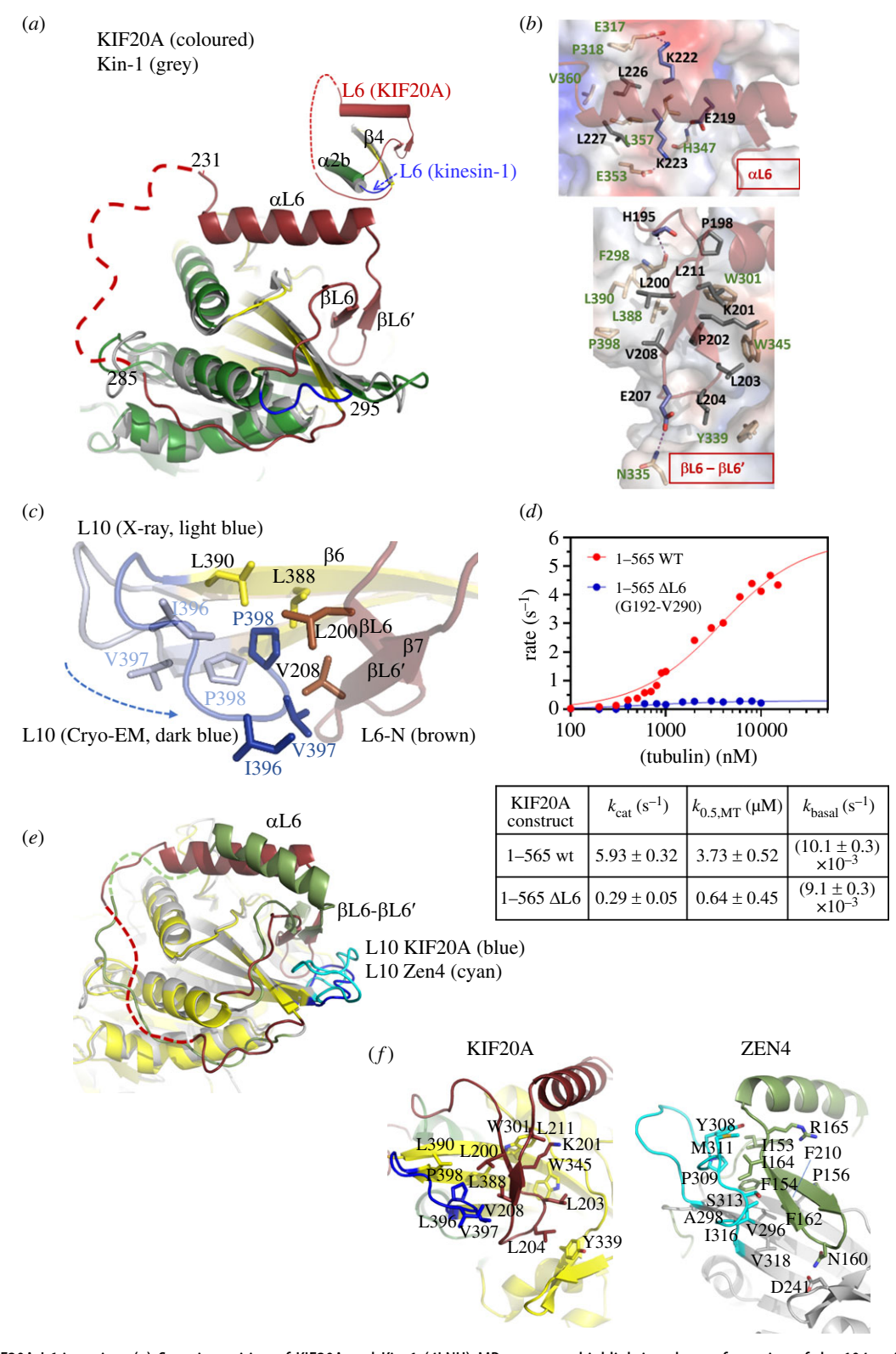


**Figure 3.** The KIF20A L6 insertion. (*a*) Superimposition of KIF20A and Kin-1 (4LNU) MD structures highlighting the conformation of the 104-residue-long KIF20A L6 (brown), in comparison to the Kin-1 L6. (*b*) Interaction of the 192–232 (L6-N) fragment of the L6 insert with the MD core establishing several hydrophobic contacts with the core: the αL6 portion (top), and the βL6-βL6′ fragment (bottom). (*c*) Variation in the conformation of L10 between the X-ray and cryo-EM structure, due to a crystal contact. I396, V397 and P398 are closer to V208 in the cryo-EM structure. (*d*) Microtubule-stimulated ATPase for monomeric 1–565 constructs, wild type (wt) or L6 insert-depleted ( $\Delta$ L6: removal of 192–290 fragment). (*e*) Superimposed KIF20A and Zen4 structures highlighting the differences between the positioning of their respective loop L6 relative to the MD core. The cryo-EM KIF20A structure was chosen for this comparison. (*f*) The βL6-βL6′ fragment of the L6 loop interacts tightly with the MD core in KIF20A L6 (brown, left), whereas it does not in Zen4 L6 (green). L10 (blue for KIF20A, cyan for Zen4) is also highlighted to indicate their differences in size, and their influence on L6 positioning in Zen4, not observed in KIF20A.

to the MD core. The L6-N makes additional interactions with L10 in the cryo-EM map that are not possible in the crystal structure. The difference is due to a bias in the  $\beta$ 6-L10- $\beta$ 7 conformation in the X-ray structure that is involved in crystal

packing contacts (electronic supplementary material, figure S5a). The common interactions between L6-N and MD core residues are particularly well defined in the crystal structure, showing multiple hydrophobic contacts (figure 3b), especially

in the βL6-βL6' region (figure 3b, bottom). Hydrogen bonds and salt bridges (via residues all Glu219, all Lys222 and <sup>αL6</sup>Lys223) are also involved in stabilizing interactions of the αL6 helix with the motor core (figure 3b, top). A large surface, which is exposed in other kinesins, contains hydrophobic residues to accommodate L6-N in KIF20A (figure 3b; and arrows in electronic supplementary material, figure S1). In the cryo-EM structure, the closer proximity between the L10 loop and βL6-βL6' hairpin appears to reinforce further these hydrophobic contacts, with the inclusion of L10 Ile396 and L10 Val397 in the <sup>L6</sup>Val208 hydrophobic network (figure 3c).

Note that since most of these interactions are apolar, small variations in the L6-N side chain interactions with the MD core might be possible for adjusting potential rearrangements of the MD core during the motor cycle although they might influence the rate of these rearrangements. This long L6 element in Kin-6s thus provide constraints on the conformation of the central β-sheet that are quite distinct from those found in other kinesin subclasses, in which a 5–6 residues L6 linker connects the  $\alpha 2$ helix and the β4 strand.

The MD structure of only one other Kin-6, the KIF23 homologue Zen4 from Caenorhabditis elegans, has been obtained at high resolution [29]. Like other Kin-6s, Zen4 possesses a characteristic insertion in L6, which is, however, 47 residues shorter than that of KIF20A (electronic supplementary material, figure S6). Although both L6 inserts contain an N-terminal  $\beta$ -hairpin followed by an  $\alpha$ -helix and a C-terminal disordered segment, the folded portions of the two L6 inserts do not superimpose (figure 3e), which is consistent with a low similarity between their sequences (electronic supplementary material, figure S6). In fact, in Zen4, the β-hairpin is not inserted between the loop L8 and the central  $\beta$ -sheet like in KIF20A, but lies more at the surface and establishes numerous interactions with a specific Zen4 insertion in L10 (figure 3f). Consequently, the L6 folded region establishes different contacts with the MD core, indicating that L6 may influence mechanochemistry in a different way in Zen4 compared to that in KIF20A.

With minimal conformational adjustments such as those revealed by our comparison between the cryo-EM and the crystallographic structures presented here, the L6-N fragment likely follows the rearrangements of the MD during the motor cycle. Furthermore, the L6-N β-hairpin region is sandwiched between the L8 loop at the interface with the microtubule on one side and the distal β6-L10-β7 region of the plus subdomain on the other side. These additional contacts made by L6-N with the \beta5a-\beta5b hairpin of the L8 loop (electronic supplementary material, figures S1, S5B) suggest that L6-N can influence the KIF20A association with microtubule or the rearrangements of the motor while bound to the track, since L8 is involved in microtubule binding [25,35]. In addition, L6 provides a bridge between the plus and minus subdomains through a hydrophobic cluster between the L6-N residue Leu194 and residues from both subdomains (electronic supplementary material, figure S5c), indicating that L6 can influence the re-orientation of subdomains during motor function. Consistently, shortening of L6 to a 5-residue linker as in Kin-1 (ΔL6, removing aa 192–290) drastically affects ATPase steady-state parameters of a fully active monomeric construct (1-565), with 20-fold reduction of the  $k_{\text{cat}}$  (figure 3d), leading to only 32-fold microtubuleactivated ATPase for  $\Delta L6$ , versus 600-fold microtubuleactivated ATPase for WT 1-565. As predicted from the structure, these kinetic studies confirm the role of L6 in the transient rearrangements of KIF20A during the motor cycle.

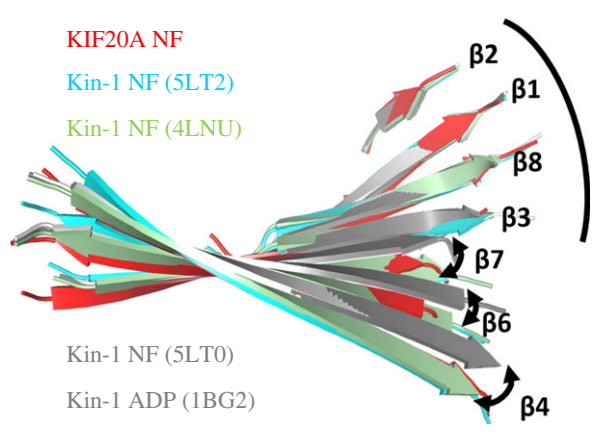
The long L6 loop is thus a structural element that plays an important role in the divergence of KIF20A mechanochemistry from that of other kinesins. Our structures now provide the grounds for guiding detailed future investigations defining its precise role along the motor cycle and for the function of this kinesin in cells.

# 2.3. KIF20A adopts a stable open conformation independent of microtubule binding

Only a small subset of kinesin MDs have been successfully crystallized in the open state in the absence of microtubules (two correspond to kinesin-1 mutants with impaired nucleotide binding (PDB, 5LT3, 5LT4), another is a particular crystal form of a kinesin-1 (PDB, 5LT2) that can also be found in a semi-closed apo state in another crystal form (PDB, 5LT0)). In this state, the NBS is highly solvent exposed, and the switch loop residues are maximally separated from the P-loop, as compared to closed or semi-closed states (electronic supplementary material, figure S7). Here we show that the overall KIF20A conformation is not affected by microtubule binding (rmsd = 0.73 Å of 286 aligned C $\alpha$  between the crystal and the cryo-EM structures) (figure 2a). Importantly, the NBS is open in both cases, indicating that microtubule binding does not induce NBS opening, unlike what has been observed in other kinesins [30,33,36]. We also found that addition of 5-10 mM Mg<sup>2+</sup>·ADP did not disrupt the possibility to crystallize KIF20A in the same conformation. No nucleotide density or ordering of the NBS was visible in the electron density maps in this case. Thus, the structures presented here are in line with our previous kinetic data showing that, as opposed to other kinesins, KIF20A has a high tendency to release the bound Mg<sup>2+</sup>·ADP [25]. SAXS data however indicate that the scattering curve differs when 5 mM Mg<sup>2+</sup>·ADP is added (electronic supplementary material, figure S8). Altogether, these data suggest that KIF20A likely does not stay in the open state in the presence of Mg<sup>2+</sup>·ADP when detached from microtubule, although the open state is particularly stabilized for this kinesin when no nucleotide is bound, even in the absence of microtubules. Interestingly, Zen4, another Kin-6, has been crystallized in a semi-open conformation in the absence of tubulin or microtubules [29].

With our high-resolution structure, we next deciphered what could lead to this unusual stabilization of the open form, a conformation usually populated when kinesins are bound to microtubules. The highly exposed KIF20A NBS is associated with a β-sheet conformation among the most twisted in kinesins, a conformation similar to that of the tubulin-bound NF Kin-1 (4LNU [32]) (figure 4a), or to that of the microtubule-bound NF Kin-3 KIF14 [30]. Characteristic of these open conformations is also an outward position of the  $\alpha 0$  helix (figure 4b,c). Molecular dynamics simulations previously predicted that the α0 helix mobility influences ATP recruitment [39].

KIF20A-specific residues are likely to contribute to the stabilization of the open KIF20A NBS observed in our structures (electronic supplementary material, figure S9). For example, in Kin-1, the twist of the central  $\beta$ -sheet of the NF state is prone to explore at least two different conformations (figure 4a) [37], one of which corresponds to the conformation of the ADPbound crystal structure (1BG2 [31]). In KIF20A, the  $\beta 3$  strand



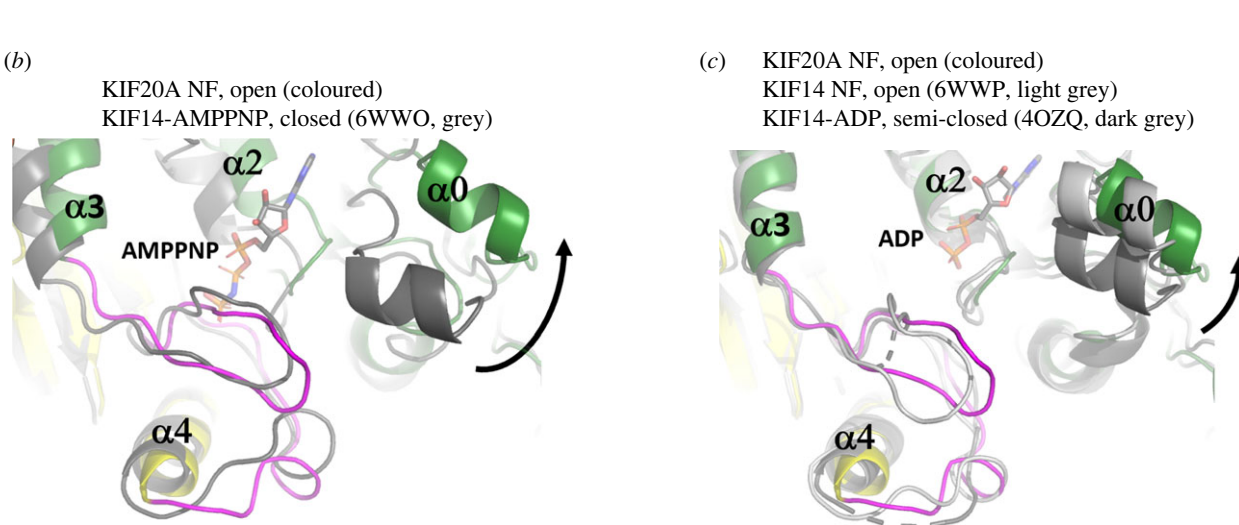


Figure 4. KIF20A exhibits an open nucleotide binding site (NBS). (a) Twist of the central β-sheet of NF KIF20A compared to that of other NF structures of Kin-1 [32,37]. (b,c) Comparison of KIF20A with the monomeric closed state (b), semi-open, and open states (c) of the Kin-3 KIF14 [30,38], showing a KIF20A NBS as open as in the microtubule-bound NF structure of KIF14. The microtubule-binding elements of the different MD structures were aligned for this comparison.

residue Trp153 appears to constrain the central  $\beta$ -sheet in a highly twisted conformation, most similar to the tubulinbound Kin-1 NF structure (electronic supplementary material, figure S9a-c). A bulky residue at this position is only found in the KIF20A and KIF20B sequences while other kinesins have small side-chain residues, which is more favourable for this transition (electronic supplementary material, figure S10). This could contribute to the preference of KIF20A for an open NBS state.

Likewise, the outward conformation of the  $\alpha 0$  helix results from the specific sequence of KIF20A. In microtubule-free Kin-1 bound to ADP, the inward position of  $\alpha 0$  is stabilized by several intramolecular interactions that cannot be established by the homologue residues in KIF20A (electronic supplementary material, figure S9d,e). In addition, the insertion of Glu82 into the L1 loop (electronic supplementary material, figure S1) is not compatible with the inward conformation of the  $\alpha 0$ helix since this would lead to charge hindrance or disruption of hydrophobic contacts and exposure of the corresponding residues (electronic supplementary material, figure S9e,f).

In addition, Kin-1 Arg190, which has been previously described to be part of the 'Mg-network' [40], is important for an adequate stabilization of the nucleotide-associated Mg<sup>2+</sup> (electronic supplementary material, figure S9g). This residue corresponds to Gln365 in KIF20A, and its side chain is too short for stabilizing a strong Mg<sup>2+</sup> coordinating network (electronic supplementary material, figure S9h). Therefore, Mg<sup>2+</sup>·ADP coordination is probably different in KIF20A compared to Kin-1. Likewise, Kin-1Gln86 is involved in the conformational stabilization of the P-loop (electronic supplementary material, figure S9i). Val160 occupies this position in KIF20A, which should lead to a less firm anchoring of the P-loop by the  $\alpha6$  residues and therefore a less stable association with the nucleotide (electronic supplementary material, figure S9j). In addition, the long L6 loop and the C-terminal extension could also participate in the stabilization of this open state.

Interestingly, from a comparison between kinesin sequences from all 14 classes, Trp153, Val160 and Gln365 are found only in Kin-6s. None of the equivalent positions in other classes harbour these residues. Instead, the equivalent Kin-1 residues are strongly conserved in other classes (electronic supplementary material, figure S10). This suggests an evolutionary rupture between Kin-6s and other classes regarding the role of these residues in tuning the motor mechanochemical cycle.

# 2.4. KIF20A is a slow motor with striking specificities in the influence of microtubules for its allosteric conformational rearrangements

To get insights into how these peculiar features of KIF20A mechanistic elements translate into function, we performed surface-gliding assays at room temperature (23°C) with a

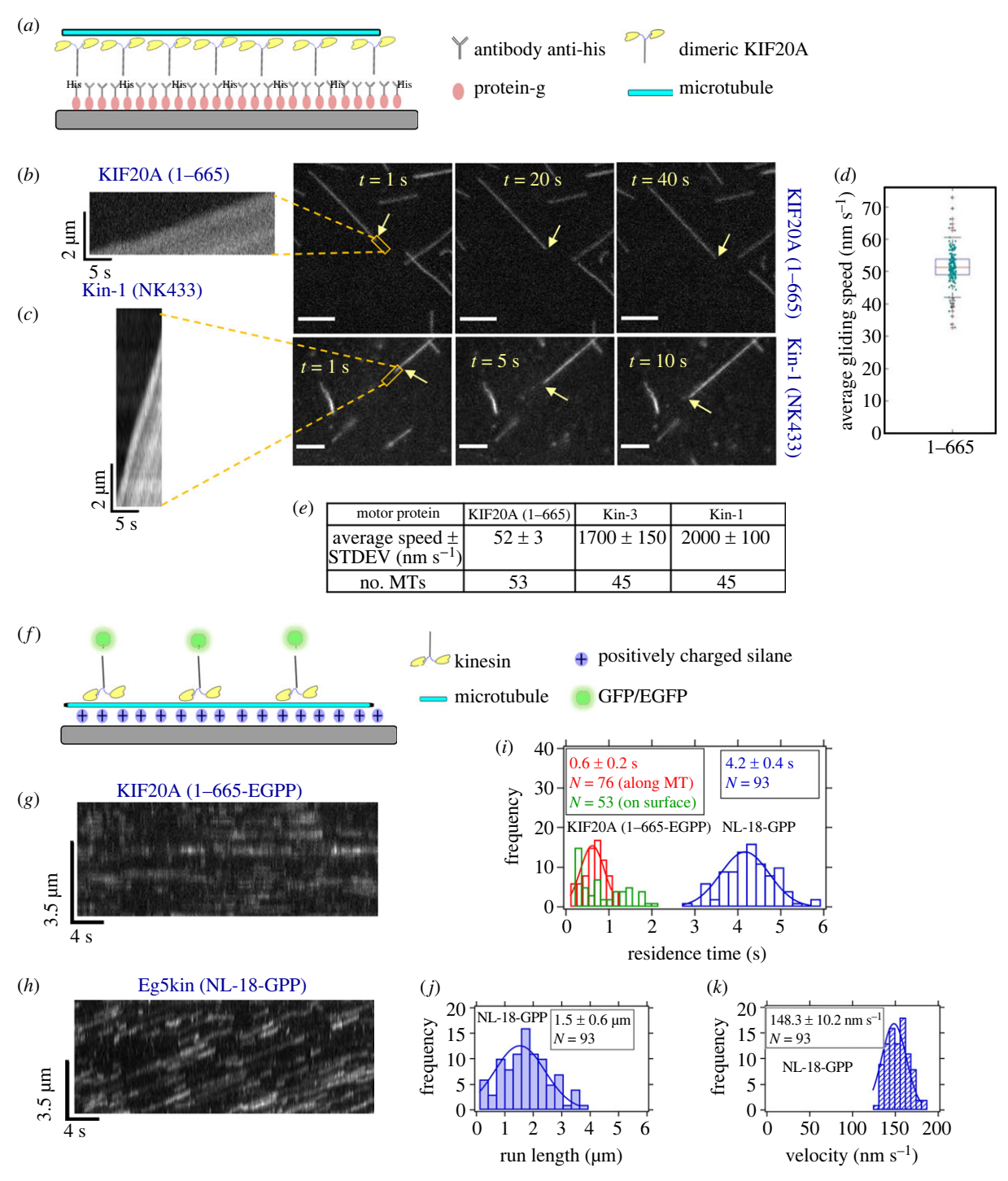


**Figure 5.** Surface gliding and single molecule motility of KIF20A 1–665. (*a*) Schematic: TMR-labelled microtubules were propelled by specifically attached motors. (*b*) Consecutive snapshots of TMR-labelled microtubules propelled by KIF20A 1–665 motors (electronic supplementary material, movie S1) at saturating ATP (2 mM) (scale bars: 5 μm). A kymograph of single TMR-labelled microtubule propelled by collectives of KIF20A 1–665 is shown on the left. Yellow arrows point towards the end of the microtubule being tracked. (*c*) Consecutive snapshots of TMR-labelled microtubules propelled by Kin-1 (NK433) as control (scale bars: 5 μm). A kymograph of single TMR-labelled microtubule propelled by collectives of Kin-1 is shown on the left. All recordings at 10 frames per second. Orange rectangles show where kymographs were recorded. Microtubule-gliding velocities were determined by fitting kymographs (electronic supplementary material, figure S11a). (*d*) Graphical representation of gliding speeds produced by the constructs in (*b*). (*e*) Average gliding speeds of KIF20A 1–665 and controls. (*f*) Schematic of the single-molecule TIRF experiment, in motility buffer, 2 mM ATP. Frame rate: 10 s<sup>-1</sup>. Kymographs generated in ImageJ. (*g*) Kymographs of 1–665-EGFP dimeric motors appearing on surface-immobilized microtubules (electronic supplementary material, movie S5), bulk motor concentration: 20 nM (2 experiments). (*h*) GFP-labelled Kin-5 dimeric motors (Eg5kin-NL-18, see Methods) landing and moving on microtubules, bulk motor concentration 20 nM (2 experiments) (electronic supplementary material, movie S6). (*i*) Single-molecule dwell times. (*j,k*) Run lengths and velocities, respectively, for Kin-5 control, measured from the kymograph in (*h*).

His-tagged dimeric motor construct (1–665) (electronic supplementary material, figure S3), attached at high densities to a coverslip by anti-His antibodies (figure 5*a*; electronic supplementary material, figure S11). Two controls were also examined: fast dimeric Kin-1 (*Neurospora crassa N*Kin-1) and Kin-3 (*C. elegans* UNC104 U653) constructs (figure 5*b-e*;

electronic supplementary material, movies S1–S3). The KIF20A constructs produced gliding speeds ( $51 \pm 5 \text{ nm s}^{-1}$ ) approximately 40 times slower than *N*Kin-1 or the Kin-3 UNC104 U653 constructs ( $2000 \pm 100 \text{ nm s}^{-1}$  and  $1700 \pm 100 \text{ nm s}^{-1}$ , respectively; figure 5b–e). Interestingly, gliding speeds in a similar range have been measured for Zen4

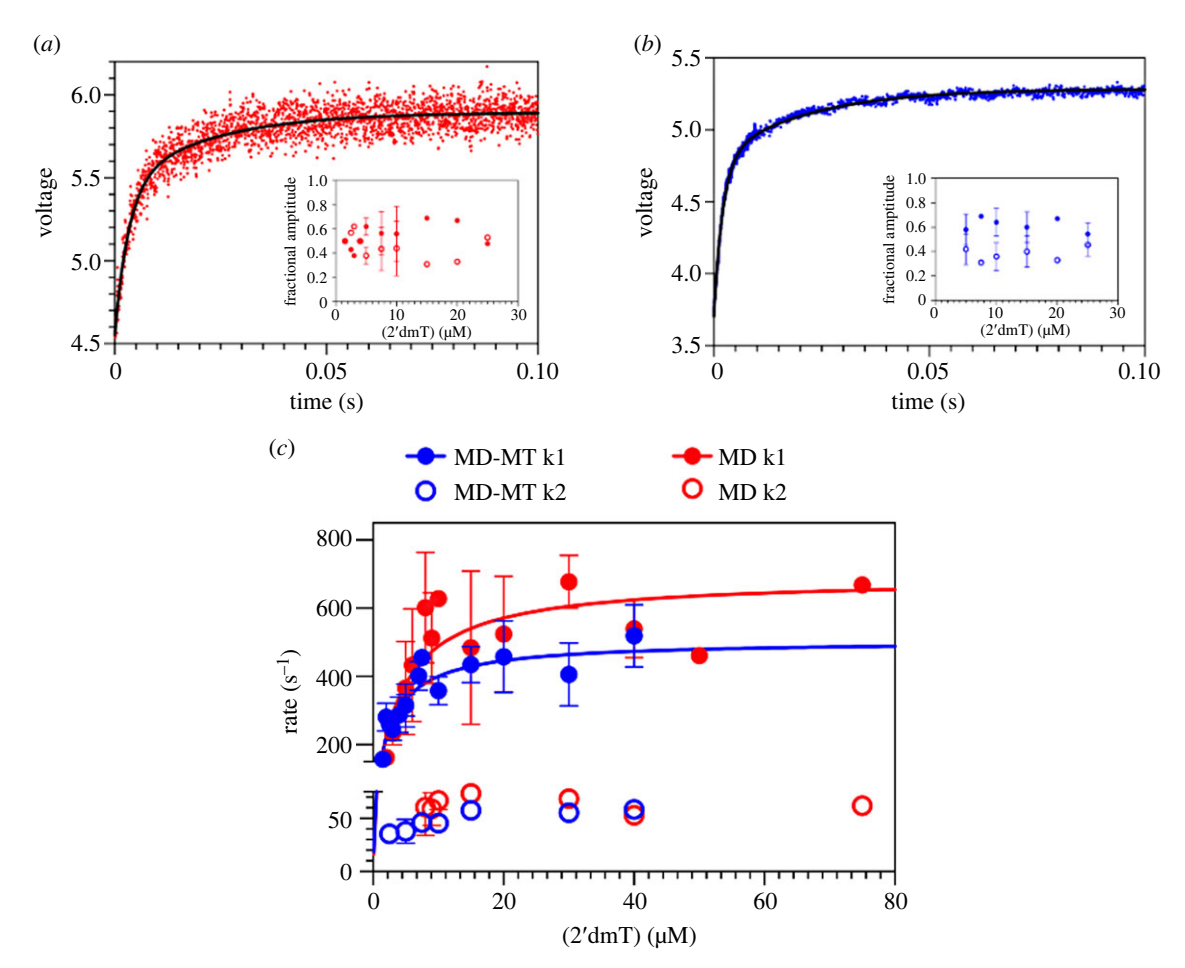


**Figure 6.** Kinetic properties of monomeric constructs of KIF2OA, revealing the involvement of the N-terminal extension and long NL in its activity. (a) Fluorescence transient produced by mixing NF MD with 20 μM of 2′dmT. The fluorescence increases in two phases. The amplitudes of these two phases are depicted in the inset (closed red, fast phase; open red, slow phase), are nearly equal in magnitude and show little dependence on [2′dmT]. (b) Fluorescence transient produced by mixing {NF MD}:microtubule complex (1 : 4 concentration ratio) with 20 μM of the fluorescent ATP analogue 2′dmT. The fluorescence increases in two phases. The amplitudes of these two phases are depicted in the inset (closed blue, fast phase; open blue, slow phase), are nearly equal in magnitude and show little dependence on [2′dmT]. In (a) and (b), the relative amplitudes for the fast phase ranged from 40 to 60% of the total amplitude (closed circles in insets). (c) Plots of the binding rates of the fluorescent ATP analogue 2′dmT to the 1–565 KIF2OA MD construct in the presence of microtubules (1 : 4 ratio (MD:microtubules), blue) and MD alone (red). Fitting to a bi-exponential rate equation shows rate constants  $k_1$  and  $k_2$  that are similar and thus insensitive to the presence of microtubules.

[29], as well as other Kin-6 s including all three human members (KIF23, KIF20A and KIF20B) [24], suggesting that this is a class-specific feature. This slow *in vitro* motor activity most likely results from the uncoupling of allosteric communication between nucleotide- and microtubule-binding events previously reported [25], that our structures emphasize.

To determine if our dimeric KIF20A constructs are processive motors, we performed single-molecule fluorescence motility assays on surface-immobilized microtubules. The labeled KIF20A (1-665-EGFP) construct moved microtubules in gliding assays (electronic supplementary material, figure S12, movie S4). In single-molecule assays (figure 5f), however, kymographs along a surface with immobilized microtubules were indistinguishable from those recorded along a microtubule-free stretch of substrate next to a microtubule (figure 5*g,i*; electronic supplementary material, movie S5). We therefore could not detect binding or movement of individual motors. In the same assay, a tail-less dimeric Kin-5 motor used as control moved processively (figure 5h-k; electronic supplementary material, figure S12, movie S6), as reported in the literature [41]. These results indicate that the dimeric KIF20A construct missing the C-terminal tail is not processive. Note that it is common for non-processive motors to promote motility in gliding assays due to collective propulsion by

many motors [42]. These results are largely consistent with the data obtained with a human KIF20A tail-truncated construct (1–720) [24] where only few events detected processivity using slow imaging rates and long imaging times.

We next compared the kinetics of ATP binding to 1-565 KIF20A MD using the fluorescent ATP analogue 2' deoxy 3' MANT-ATP (2'dmT). Data were acquired in the presence or absence of microtubules to probe whether the open NBS suggested by structural studies indeed facilitates binding of nucleotide compared to other kinesins. Mixing 2'dmT with NF preparations of MD or of a 1:4 MD-microtubule complex produced a biphasic fluorescence increase (figure 6a for MD and figure 6b for MD-microtubule), defining fast and slow phases. The presence of two phases in the fluorescence transient implies two conformational changes occur following formation of a collision complex between the catalytic site and 2'dmT. Whether these steps occur sequentially or independently of each other is reflected in the dependence of the rate of each phase on ligand concentration [43]. For both MD (red) and MD-microtubule complexes (blue) (figure 6c), the faster phase shows a clear hyperbolic dependency of rate on [2'dmT], defining maximum rates and apparent second order rate constants for 2'dmT binding, respectively, of  $688.5 \pm 92.0 \,\mathrm{s}^{-1}$  and  $169 \,\mu\text{M}^{-1} \,\text{s}^{-1}$  for MD; and  $505 \pm 42 \,\text{s}^{-1}$  and  $193 \,\mu\text{M}^{-1} \,\text{s}^{-1}$  for

MD-microtubule. The rate constant for the slower phase for MD shows no significant dependency on [2'dmT], as expected for sequential conformational changes, and averages 60–70 s<sup>-1</sup> (figure 6c, open red circles). While the rate of the slower phase for a MD-microtubule complex shows a very modest dependency on [2'dmT] at low ligand concentrations (figure 6c, open blue circles), we conclude that these two conformational changes are likely sequential in a MD-microtubule complex as well.

As we previously reported for the shorter 25–520 construct [25], microtubule binding has little effect on the kinetics of ATP binding to or release from the catalytic site of the 1–565 KIF20A MD. However, one important difference is that the apparent second-order rate constant for 2'dmT binding to the 1-565 MD is 10-20 fold faster than that for the shorter 25-520 MD version [25], and 20-50 fold faster than corresponding values for Kin-1 or Eg5 [44]. This suggests that the catalytic site in NF KIF20A is considerably more accessible to nucleotide than in other kinesins. This is consistent with our finding that KIF20A adopts a stable NF state with a wide-open active site, as discussed above (figure 4). In addition, these results suggest a critical role of the N- and C-terminal extensions in KIF20A in stabilizing this NF conformation or in influencing the interaction with microtubule.

## 2.5. Microtubule-binding interface: comparison with other kinesins

The KIF20A MD interacts with the microtubule through similar areas to those observed in other kinesin-microtubule complexes (L8, L11, H4, L12, H6). However, residue differences in these areas result in different conformations of the interacting regions (figure 7).

The areas of contact with tubulin (the 'footprint') are also similar to that observed in motile kinesins with most of the contacts made with the terminal helix-12 of  $\alpha$ - and  $\beta$ -tubulin. However, KIF20A specific residues in these areas result in different contacts (figure 7c,d; electronic supplementary material, figure S13) and a different overall orientation of the MD relative to tubulin (figure 7b) as compared to other kinesins. This difference was mentioned by comparison of Kin-1 and low resolution KIF20A structures [25]. Here we show that the shift is even more pronounced when the microtubule-bound KIF20A is compared to Kin-3 (figure 7b) [30]. In addition, to these interactions, the KIF20A elongated loop L2 and the minus-end pointing NL of this NF structure locate very near the microtubule interface and form salt bridges and hydrophobic interactions with  $\alpha$ -tubulin (figure 7c).

# 2.6. The role of the neck-linker initial segment in tuning neck-linker directionality

In both the X-ray and cryo-EM open structures, the KIF20A NL is oriented towards the microtubule minus-end, similar to what was previously described for Zen4 [29]. In these Kin-6s, the 'NL initial segment' (NIS) [46] is docked onto the MD core by forming a β-strand interacting with β1c (figures 1b, 8a,b; electronic supplementary material, figure S14a). Interestingly, the structure of the ADP-bound Kin-10 KIF22 (6NJE, Walker et al., unpublished) also exhibits a similar NIS conformation, demonstrating that this backward NIS docking is not restricted to Kin-6s and can occur when ADP is bound in a semi-closed NBS state. For other kinesins,

backward docking was in fact observed for the lead head only in the particular condition that two heads would be bound to microtubule. We thus analysed what promoted backward docking in KIF20A independent of load.

The backward docking of the NIS leads to a C-terminal shortening of the  $\alpha6$  helix by approximately 1.5 turns as compared to post-power-stroke structures (figure 8f). The unwound residues are from the NIS (L502-L506) [46] and from a short preceding pre-NIS linker (F499-L502). The pre-NIS linker sequence is adjusted to allow docking of the NIS immediately following the  $\alpha6$  helix promoting the NIS interaction as a supplemental  $\beta$ -strand to the peripheral β-sheet made of β1a, β1b and β1c via five intra-strand hydrogen bonds (figure 8b). Interestingly, the class-1 cryo-EM map indicates how the NL after NISLeu506 continues to form apolar interactions with the MD for at least 9 residues (until Leu514). Gly515 and Pro517 promote a turn in the NL so that the following residues mainly form apolar contacts with the microtubule (figure 7c). In most of the other known pre-power-stroke plusend kinesin MD structures (NF or ADP-bound with either an open or semi-closed NBS), this region stays helical until the end of the NIS (KIF5B Lys323, which would correspond to KIF20ASer504) (electronic supplementary material, figure S14a).

In fact, recent high-resolution cryo-EM structures of the Kin-3 KIF14 [30] show that when the two heads of dimeric constructs bind to microtubule, the NL of the leading head is oriented backwards through the formation of an extra strand interacting with \beta1c (figure 8e; electronic supplementary material, figure S14b). However, this backward docking does not occur when only one head is bound to the microtubule. Strikingly, in this case the residues involved in the additional strand are not from the NIS but from the NL [30] (figure 8e,f). This suggests that the tension between the two heads simultaneously attached to the microtubule can also result in a stabilized backward orientation of the NL, via a  $\beta$ -sheet interaction with  $\beta1c$  in other kinesins. This strain is not a prerequisite for the NIS docking in KIF20A, since this conformation is stable in the single-head structures described here. The fact that the backward docking of the NIS is observed out of the context of a constrained microtubulebound dimeric kinesin configuration implies that elements within the MD favour this conformation.

We find that one critical element is the pre-NIS sequence. In both KIF20A and Zen4 structures, the side chains of the NIS residues do not significantly participate in the backward-docking stabilization. In fact, in Zen4, the NIS starts one residue earlier in sequence, with the preceding  $\alpha 6$  helix shorter by one residue, and the pre-NIS linker thus adopts a different conformation (figure 8c). The conserved feature of these structures is the positioning of an alanine of the pre-NIS linker (KIF20A Ala501 and Zen4 Ala420) so that it occupies the same hydrophobic pocket, that we call the pre-NIS cavity, adapted for hosting only a small side chain (Ala or Gly) of the pre-NIS (figure 8c). A similar pre-NIS alanine residue is also found in the ADP-bound Kin-10 KIF22 structure that displays a similar NIS backward docking (figure 8f).

By contrast, when examining the NIS sequence from other plus-end kinesins, the presence of an arginine-alanine-lysine 'RAK' motif [47] appears to favour an extended α6 helix (electronic supplementary material, figures S14a,c, S15). The lysine residue of this motif (Kin-1Lys323) lies in proximity to the Kin-1 Asp49 when the NIS stays helical. When conserved in plus-end kinesins, this aspartate can thus contribute to the

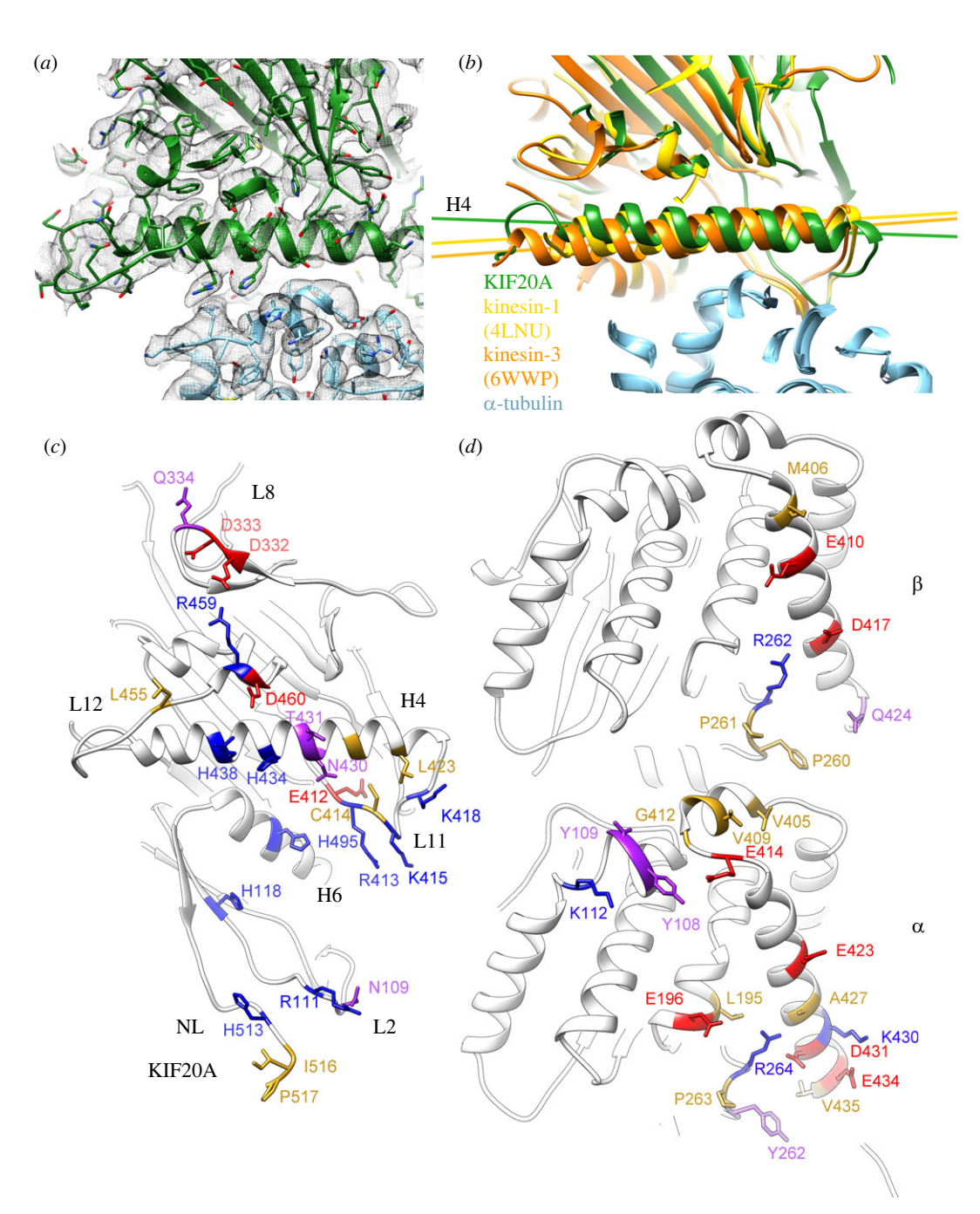
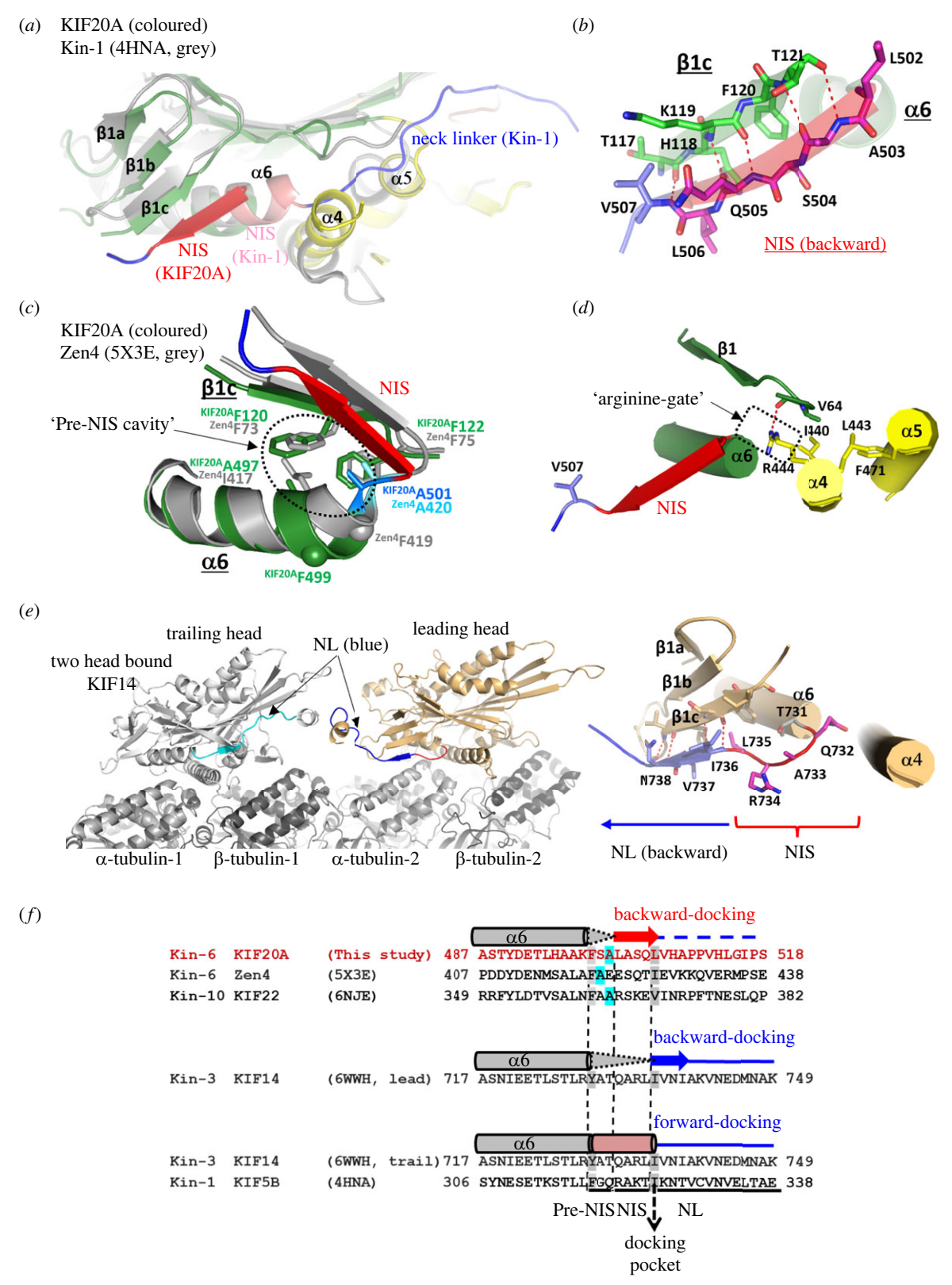


Figure 7. Interface kinesin—tubulin. (a) KIF20A-microtubule interface (class-1) near the KIF20A α-helix 4 (H4). KIF20A MD in green, tubulin in light blue and corresponding cryo-EM density isosurface as a semi-transparent grey mesh. (b) The KIF20A MD in the microtubule complex is rotated relative to the MDs in the Kin-1 and the Kin-3 microtubule complexes. All three microtubule or tubulin complex structures are aligned to their corresponding  $\alpha$ -tubulin subunits. KIF20A MD in green, Kin-1 (KIF5B) MD in yellow, Kin-3 (KIF14) MD in orange, and  $\alpha$ -tubulins in light blue. Views in (a) and (b) are from the microtubule plus end towards the minus end. (c) View of the KIF20A-microtubule interface from the microtubule. (d) View of the KIF20A-microtubule interface from the KIF20A MD. In (c) and (d), KIF20A and microtubule residues making contacts at the interface are shown as stick atom representations and coloured according to the residue properties (negative in red, positive in blue, polar in purple and hydrophobic in yellow). Residues making contacts at the interface were identified using the UCSF-Chimera routine 'find clashes/contacts' [45].

winding and stabilization of the extended α6 helix. However, both the aspartate and the 'RAK' motif are missing in Kin-6s and the residues found at these positions are inadequate to interact with one another (electronic supplementary material, figure S15). The absence of this α6 helix stabilization in Kin-6s can thus favour unwinding and backward docking of the NIS. In the case of the lead head of KIF14, Thr731 cannot fit in the pre-NIS cavity and the following NIS 'QAR' residues found in place of the 'RAK' motif cannot dock on β1c (figure 8e,f). In fact, both the pre-NIS and NIS do not wind as part of  $\alpha 6$ , but they form a disordered undocked linker.

The backward docking to extend the β1a-β1c β-sheet in fact only involves NL residues via the formation of three hydrogen bonds (figure 8e).

In the nearby α4 helix, the KIF20A Arg444 (the equivalent of the Zen4 'arginine gate' Arg363 [29]) provides a large side chain that seems incompatible with the helical conformation of the last turn of the  $\alpha$ 6 helix in this open state (figure 8d). Furthermore, Arg444 stabilizes this state by making a strong hydrogen bond with the carbonyl of Val64, which anchors the  $\alpha 4$  helix to the MD N-terminal fragment and blocks access to the pocket that accommodates forward



**Figure 8.** Conformation of the NL in the open state of KIF20A. (*a*) The minus subdomain of the KIF20A MD structure superimposed on that of the closed structure of human Kin-1 MD (PDB, 4HNA). The NIS elements (docked backward in KIF20A (red) and a part of the helix  $\alpha$ 6 in Kin-1 (salmon)) are found in opposite directions. NL fragments are coloured in blue. (*b*) β-Sheet interactions between KIF20A NIS and the β1c strand, from the minus subdomain. (*c*) Comparison of the  $\alpha$ 6 helix, pre-NIS and NIS found in pre-power-stroke structures. KIF20A is compared to Zen4. The KIF20A  $\alpha$ 6 helix is one residue longer than that of Zen4. In KIF20A, a serine, Ser500, is present between the last  $\alpha$ 6 residue (Phe499) and the pre-NIS residue Ala501. In Zen4, the equivalent phenylalanine is directly followed by the pre-NIS alanine (Ala420) and its positioning in the pre-NIS cavity requires distortion of the end of the  $\alpha$ 6 helix. Following these pre-NIS residues, a similar β-sheet interaction allows the docking of the NIS element onto the β1c strand. (*d*) Details of the KIF20A closed docking pocket showing the side chain Arg444 (Arg-gate) that prevents the NIS fragment from winding and elongating the  $\alpha$ 6 helix. (*e*) Structure of a dimeric construct of the Kin-3 KIF14, in a two-head bound microtubule form, with the leading head exhibiting a backward orientation of the NL via a β-sheet interaction between its proximal NL residues (Ile736, Val737 and Asn738) and the β1c strand. (*f*) Structure-based sequence comparison of the NIS-NL fragments of KIF20A and other plus end kinesins with a similar backward docking of either their NIS or proximal NL fragment on β1c. The sequence of the equivalent fragment of the closed structure of Kin-1 is also shown, to indicate the NIS residues that extend the  $\alpha$ 6 helix (up to the 'docking pocket' position) when the NL is docked forward.

docking of the NL during the power stroke (figure 8d) [35,48,49]. Interestingly, the residue found at the 'arginine gate' position of the  $\alpha 4$  helix is a conserved arginine in Kin-6s but not in other classes, in which a residue with a short aliphatic side chain (Val, Ala; Ala129 in Kin-1) or a small polar side chain (Asn312 in KIF22) is found (electronic supplementary material, figure S15). Therefore, a large (e.g. KIF20A Arg444) and/or polar (e.g. KIF22 Asn312) residue at the 'arginine gate' position disfavours the helical conformation of the NIS, increasing its propensity to be docked backwards. Thus, the nature of the residues that can interact or clash with the pre-NIS cavity as well as those involved in stabilization of the helical form of the NIS likely contribute to tune the NIS docking/unwinding or rewinding.

In conclusion, the pre-NIS and the NIS sequences, as well as the surrounding residues involved in their stabilization differ among kinesins and likely cooperate to modulate the NIS conformation, and therefore the kinetics of transitions for the power stroke.

## 2.7. The N- and C-terminal extensions contribute to KIF20A functionalities

The large extensions at both the N- and C-termini of the MD constitute two other distinct features in KIF20A (figure 1a; electronic supplementary material, figure S1). At the C-terminus, the NL fragment (506-553), which links the MD to the dimerization domain, is approximately 4 times longer in KIF20A than in Kin-1 (figure 9a).

Such a long NL should preclude processive high-speed motility [26,27,41,47,49–52]. Likewise, the 'cover-strand' (CS), i.e. the N-terminal fragment that assists the power stroke by forming the 'cover-neck bundle' [49,53,54], corresponds to residues 59-64 in KIF20A (electronic supplementary material, figure S1), which raises questions about the role of the 1-59 fragment. We confirmed the involvement of the KIF20A N-terminal extension with a gliding motility assay, using dimeric constructs with shortened N-terminal extension 55-665 and 25-665 (figure 9b,c; electronic supplementary material, movies S7, S8). The gliding speed measured at 23°C produced by the 55-665 construct was lower than that produced by the 1-665 construct, implying that the N-terminal extension has a role in controlling KIF20A velocity. The presence of the entire N-terminal extension appears necessary, since an intermediate truncation (25-665) displayed an even lower velocity (21 nm s<sup>-1</sup>; figure 9c). We repeated the gliding assays at 30°C to control for temperature effects and found only negligible increases in speed (electronic supplementary material, figure S16).

However, although we used the monomeric 1-565 construct that contains both the intact N- and C-terminal extensions for cryo-EM (figures 1a, 2a), no density was present for the residues 1-58 and 518-565. This indicates that the NF state of KIF20A is associated with disordered N-terminal and NL extensions, even when microtubules are present. Interestingly, while no prediction can be made for the N-terminal extension from the KIF20A-microtubule complex structure, the backward directed NL (506-517) is positioned towards the microtubule minus end in such a way that it contacts residues of α-tubulin alongside the L2 loop (figure 7). Further gliding motility assays with deletion constructs in the NL shed more light on the functional importance of specific NL residues. The first construct lacked a stretch of 15 charged residues at the C-terminal end of the NL ( $\Delta(535-549)$ ), the second lacked a further 17 residues (Δ(518–549)), leaving a NL of 16 residues, slightly longer than the 10-residue NL found in transport kinesins. The construct with the shortest NL ( $\Delta$ (518–549)) displayed a very low gliding velocity (10.6  $\pm$ 0.6 nm s<sup>-1</sup>) (figure 9b,c; electronic supplementary material, movie S9), while the gliding velocity produced by the  $\Delta$ (535– 549) deletion mutant  $(35.7 \pm 4.4 \text{ nm s}^{-1})$ ; figure 9c; electronic supplementary material, movie S10) was closer to that of the parental construct, suggesting that the charged residues at the C-terminus of the NL are not essential for the collective driving of microtubule motility. Consistently, by examining KIF20A sequences from various species, the level of conservation of the NL sequence up to residue 531 is higher than for downstream residues, indicating that within the NL, the fragment 506-531 has an important role in evolution (electronic supplementary material, figure S17).

We also confirmed the role of the N- and C-terminal extensions in modulating the kinetic properties of KIF20A with steady-state kinetics assays with different deletion constructs (figure 9d,e). Compared to the 1–565 constructs, those with shortened NLs (1–520 and 25–520) displayed an approximately 40% reduction in  $k_{\text{cat}}$  and a 2–3 fold increase in  $K_{0.5,\text{MT}}$  [25] (figure 9d,e). Reducing the length of the N-terminal extension, on the other hand, increased  $k_{\text{cat}}$  by about 70% with a modest reduction in  $K_{0.5,MT}$  (figure 9d,e). These results suggest that the N-terminal extension does not modulate the affinity of KIF20A towards microtubules. Efficient ATP hydrolysis however requires a full N-terminal extension beyond the CS as well as a much longer NL compared to other kinesins. Thus, these extensions of the MD core play essential roles in regulating enzymatic turnover in KIF20A.

# 3. Discussion

KIF20A is an atypical member of the kinesin superfamily with key roles in interphase and in mitosis. The unique and long loop insertions in its MD, as well as large N-terminal and NL extensions are likely to contribute to the cellular function of this Kin-6. Our high-resolution structure of the MD-alone or bound to the microtubule—and our functional assays reveal how these KIF20A-specific elements impact motor function. The central part of the 104-residue-long KIF20A L6 loop, the L6-M moiety, is disordered in our structures. This portion is likely to constitute a supplemental modulating element for this kinesin in cells by associating with cellular partners, either cargoes or regulatory proteins. Our structural and functional results show, in contrast, that the N-terminal sequence of L6 (L6-N) strongly interacts with the plus and minus subdomains. The KIF20A structures indicate how L6-N can influence the twist of the central  $\beta$ -sheet and the L8 loop conformation, a loop involved in microtubule binding. Thus, the L6 loop influences the KIF20A mechano-transduction and kinetics by affecting structural changes along the ATPase cycle and/or microtubule affinity. Therefore, the L6 loop emerges as a major contributor to the specialization of KIF20A. Such a role of the L6 loop echoes the modulatory role for force generation in myosin splice variants that has been demonstrated in Drosophila muscle myosin via alternative splicing in the exon 7 [55]. It is likely that this element alters the transitions of the motor cycle by impacting how the rearrangements can occur in the central β-sheet.

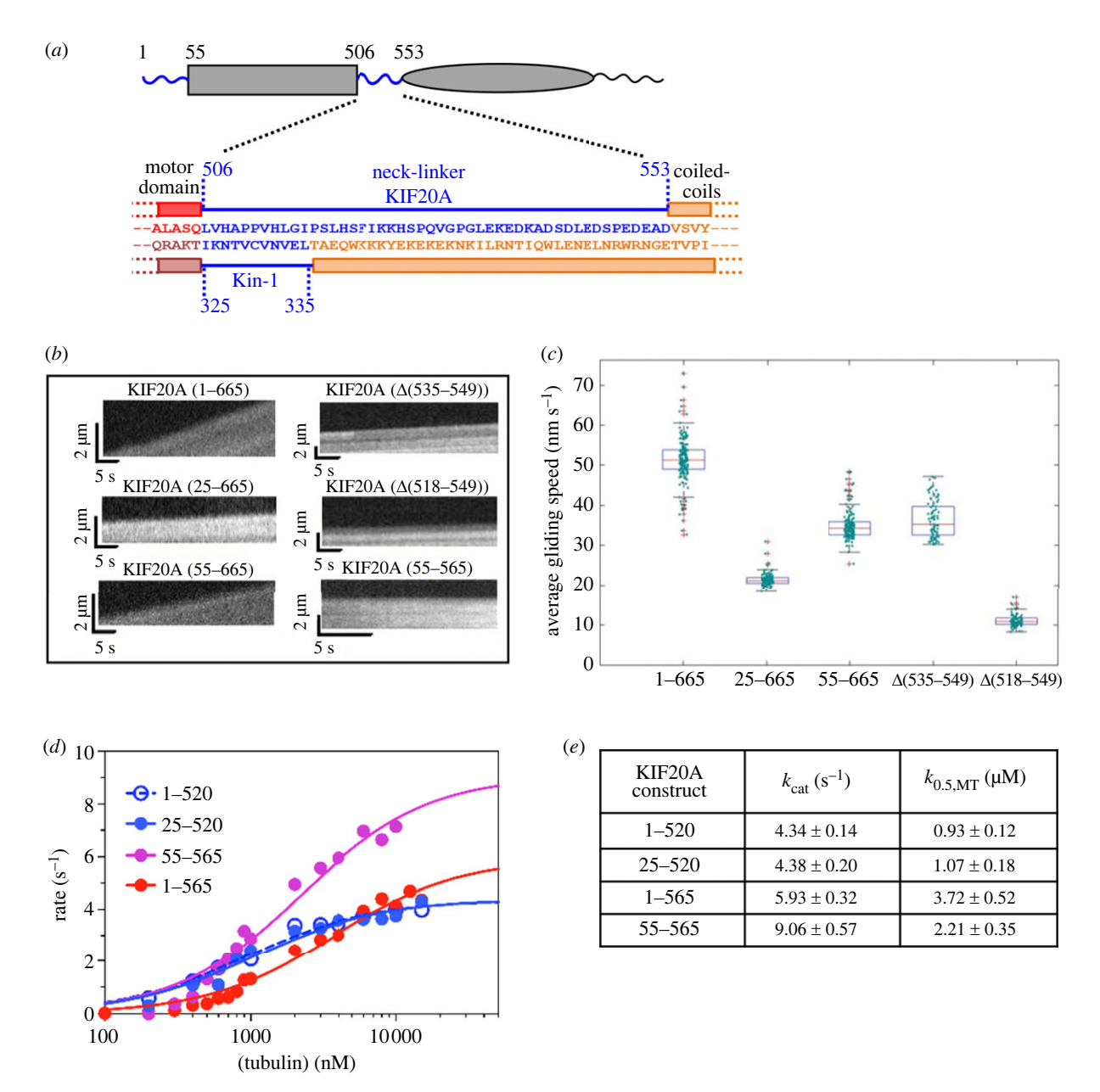


**Figure 9.** Motility and ATPase activities of different constructs of KIF20A having different truncations or deletions in the N-terminal extension or in the NL. (a) Schematic representation of KIF20A highlighting the long N-terminal and NL extensions (blue). The 48 residue-long sequence of KIF20A NL is compared to that of Kin-1 (11 residues). (b) Kymographs of TMR-microtubules propelled by the KIF20A dimeric motor constructs 1–665, 25–665, 55–665,  $\Delta$ (535–549),  $\Delta$ (518–549) and the monomeric 55–565 (control), respectively, at 23°C. The vertical axis of the kymographs represents microtubule displacement, the horizontal axis time. (c) Average gliding speeds produced by the constructs in (b). (d) microtubule-stimulated ATPase for four KIF20A monomeric constructs. (e) Steady-state parameters extracted from (d). In (d) and (e), note that the constructs 1–520 and 25–520 have been characterized previously [25] and the results have been reported here for comparison with the newly designed longer construct 55–565 and the full-length functional MD (1–565).

Strikingly, as opposed to previously studied purely motile kinesins, KIF20A adopts a pre-stroke state in the absence of nucleotide in which the NBS is as open when bound to the microtubule as when detached from the microtubule. Our structures indicate that this specific property results from differences in key residues that influence the conformations of either the  $\beta$ -sheet or the NBS. In addition, L6-N likely contributes to the stability of this open conformation. Thus, unlike other kinesins, KIF20A does not need the assistance of the microtubule to trigger the opening of the NBS that is required for ADP release [50,56,57]. With this ability to stably reach the open NF conformation, this Kin-6 is set apart from other classes of plus-end directed kinesins and—unlike other kinesins which tightly bind ADP in the absence of microtubules—displays a mechanism in which ADP can be

released before the engagement on the microtubule track (figure 10). At this point, the kinetic parameters of the different steps in the KIF20A mechanochemical cycle have not been fully established. Complete transient kinetic measurements should be conducted using a full-length MD (1–565) to precisely and accurately provide a full picture of the mechanochemistry of this kinesin. The atypical features found in the current structures indicate that the KIF20A sequence might lead to a functional adaptation best fitted for a distinct mechanical role, compared to other kinesins, in which high stability of the detached open state would be an advantage.

In addition, the C-terminal NL and the preceding NIS region further stabilize the open state by interacting with the MD while adopting a backward orientation. In this open

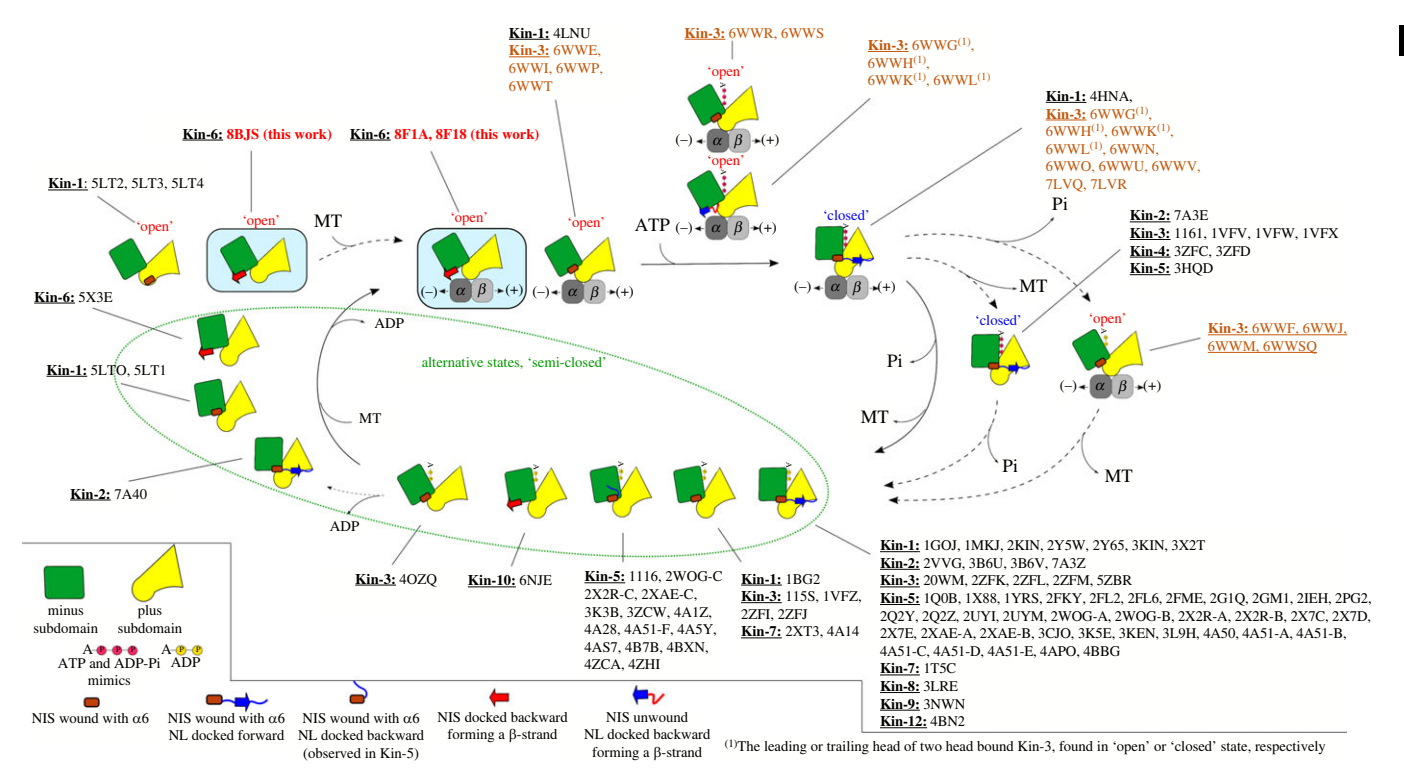


**Figure 10.** Schematic representation of the KIF20A NF state and comparison with other states of plus ended kinesins. The different states that have been observed for plus end kinesins are represented with PDB codes along a generic motor cycle. The twist of the central β-sheet is represented by different relative orientations of the minus and plus subdomains. The KIF20A structures of the current study are highlighted in red and their schematics on a light blue background. The other crystal structures reported (PDB IDs in black) are those at higher resolution than 3.7 Å. The recent high-resolution cryo-EM structures of the microtubule-bound Kin-3 KIF14 at different nucleotide states have been included (PDB IDs in orange).

state, the NIS portion of KIF20A is unwound from the α6 helix and docks on the  $\beta$ -strand  $\beta$ 1c to orient the NL towards the minus-end of microtubule, like in Zen4 [29] or in the Kin-10 KIF22 (6NJE, Walker et al., unpublished). In fact, several pieces of earlier evidence support a backward orientation of the NL in some kinesins in the NF state [29,58-61]. As demonstrated by the recent high-resolution cryo-EM study of the Kin-3 KIF14, such a backward docking is indeed found for the lead head in the two-head-bound state, albeit not in the NF state [30]. However, we find here that the NIS (the preceding sequence) can play a critical role in favouring this backward direction of the NL on a single head and without binding to a microtubule. Note that the backward docking proposed from low-resolution cryo-EM maps for Kin-5 disposes the NL on top of the β1a-β1c β-sheet, guided by a class-specific sequence conservation [59,62] (electronic supplementary material, figures S13, S14c). The docking of the NIS fragment, rather than the NL per se (as seen in KIF14) is clearly unusual among kinesins and is a characteristic of only a few kinesins that possess a residue of small side chain in the NIS. Together with the elements that control the NBS opening, the sequence elements that guide the (un)winding of the NIS and its backward docking constitute another leverage to regulate the motor mechanism and can contribute to the specific kinetics and motility properties of KIF20A. As a result, KIF20A exhibits an unusual coupling between microtubule- and nucleotidebinding events, although microtubules do activate its ATPase activity. These structural characteristics are likely to render this kinesin particularly slow as revealed by our gliding assays.

We finally found that, although largely disordered in our structures of the NF state, extensions at both N- and C-terminus of the MD are involved in KIF20A functionalities. Our kinetic

studies indicate that in KIF20A, these elements must be much longer than in other kinesins to retain normal enzymatic properties. The mechanism beyond this property remains to be investigated in detail. It is possible that the N-terminal extension expands the cover strand to assist the NL movement during the power stroke. Future structural studies of other nucleotide states will be of high interest to highlight the role of these extensions. The current models for kinesin stepping attribute an important role to the length of the NL for processivity [26,27] and imply that the long KIF20A NL should impede processive motility. Indeed, tail-less versions of KIF20A confirm that the dimerization domain alone is not sufficient for this motor to be robustly processive (figure 5f-i), which would render it unable to transport cargoes in cells [24]. Interestingly, however, another study found full-length KIF20A to be processive and characterized the influence of cargoes on the run-length [28]. How the tail fragment and physiological KIF20A partners influence KIF20A motility constitutes another fascinating area for future research on this kinesin. These need to include the proteins that are involved in KIF20A regulation and modulate its activities along the cell cycle.

For example, during the metaphase/anaphase transition in mitosis, KIF20A, bound to the CPC, acts as a transporter [28]. Plk1 phosphorylates KIF20A in its NL (Ser527), which is required for Plk1 to bind to KIF20A and reach its proper localization [20]. In interphase, KIF20A promotes membrane scission to form RAB6 vesicles at Golgi hotspots in association with myosin-2 and RAB6. At these sites, KIF20A might favour the formation of a microtubule network linked to contractile actomyosin rather than acting as a transporter since its depletion results in the appearance of elongated tubules

growing from RAB6 hot spots [6]. As is the case with many other macromolecular machines, important puzzles about the complex functions of the KIF20A kinesin in the full cellular context thus await further investigation after basic structural and functional features have been discovered.

## 4. Material and methods

#### 4.1. Protein expression and purification

The production procedure for KIF20A constructs containing the MD was derived from the preparation method for the 25-520 KIF20A construct previously studied by cryo-EM [25]. Briefly, all these constructs were cloned into pET28b with a C-terminal 6His tag and were expressed in NiCO21 (DE3) E. coli cells (New England BioLabs, Evry, France) by induction with 0.2 mM IPTG overnight at 20°C. Cells were harvested by centrifugation at  $4500 \times g$  for 20 min and lysed by sonication in lysis buffer (50 mM HEPES, pH 7.5, 500 mM NaCl, 40 mM imidazole, 0.5 mM TCEP, 0.1 mM ATP, 5 mM MgCl<sub>2</sub>, 5% glycerol and complete EDTA-free antiprotease cocktail (Roche, Boulogne-Billancourt, France)). The lysate was clarified at  $20\,000 \times g$  for 45 min at 4°C, and the impurities that were tagged by chitin binding domain were extracted on a gravity-flow column using 5 ml chitin resin (New England BioLabs, Evry, France). The target proteins were purified with HisTrap HP columns (GE Life Sciences, Velizy-Villacoublay, France). Further purification was achieved by size-exclusion chromatography in buffer containing 20 mM HEPES, pH 7.5, 150 mM NaCl, 1 mM TCEP, 5 mM MgCl<sub>2</sub>, 0.1 mM ATP. Fractions containing purified KIF20A protein were pooled and concentrated to the desired concentrations, flash-frozen in liquid nitrogen and stored at -80°C until use. All the monomeric constructs (1-520, 25-520, 55-510, 55-565, 1-565) were concentrated up to approximately 20 mg ml<sup>-1</sup> and the dimeric constructs (1-665, 25-665 and 55-665) to approximately 5 mg ml<sup>-1</sup>. To analyse the role of the neck-linker for motor properties in vitro, two variants of the 55-665 dimeric motor were designed, lacking residues 518-549 or 535-549, respectively. For the 1-565 construct used for cryo-EM, the final size-exclusion chromatography was performed with a buffer composed of 80 mM PIPES, pH 6.8, 75 mM KCl, 2 mM MgCl<sub>2</sub>, TCEP 1 mM, 1 mM EGTA, 0.1 mM ATP.

Verification of the monomeric or dimeric state of those constructs was obtained by SEC-MALS experiments with the injection of 5 mg ml<sup>-1</sup> of each protein into a Superdex 200 10/30 Increase column (GE Life Sciences, Velizy-Villacoublay, France) mounted on a HPLC Ultimate 3000 (Thermo Scientific, Waltham, MA USA) coupled to a mini-DAWN Treos and an Optilab T-rEX (Wyatt Technology, Santa Barbara, CA, USA) for MALS and refractive index measurements. Data were analysed using ASTRA 6 software (Wyatt Technology, Santa Barbara, CA, USA).

To ensure the NF state of the 55-510 construct used for crystallization, a batch was produced with the omission of nucleotide in all buffers. For crystallographic structure solution, a selenomethionine derivative of the 55-510 construct was produced using the SeMet kit from Molecular Dimensions (Sheffield, UK) using the instructions from the provider.

For control experiments, including gliding assays and single-molecule motility assays, we used a truncated dimeric Kin-1 construct from Neurospora crassa (NK433) [63], a Kin-3 construct from C. elegans (UNC-104 U653) [64,65] and a chimeric Kin-5/Kin-1 construct (chimeric Eg5Kin-NL-18) [41]. The motors were expressed using the E. coli BL21 (DE3) strain. NK433 and Eg5Kin-NL-18 were expressed and purified essentially as described previously [41]. Briefly, when bacterial growth reached exponential phase, protein expression was induced with 0.1 mM IPTG overnight at 20°C. Cells were harvested and sonicated as described above, in 20 mM NaPO<sub>4</sub>, pH 7.4, 1 mM MgCl<sub>2</sub>, 10 mM β-mercaptoethanol, 0.1 mM ATP. The target proteins were first purified by Ni-NTA affinity chromatography, then buffer-exchanged by overnight dialysis in BRB80 buffer (80 mM PIPES, pH 6.8, 1 mM MgCl<sub>2</sub>, 1 mM EGTA) supplemented with 0.1 mM ATP and 1 mM DTT. UNC-104 U653 was further purified by ion-exchange chromatography and was eluted in a ratio of 70% buffer A (25 mM PIPES, pH 6.8, 2 mM MgCl<sub>2</sub>, 0.1 mM EGTA, 0.1 mM ATP, 1 mM DTT) and 30% buffer B (25 mM PIPES, pH 6.8, 2 mM MgCl<sub>2</sub>, 0.1 mM EGTA, 250 mM NaCl, 0.1 mM ATP, 1 mM DTT). Aliquots were then snap frozen in liquid nitrogen and stored at -80°C.

#### 4.2. Microtubule preparation

For motility assays, all reagents were obtained from Sigma-Aldrich (Hamburg, Germany) unless otherwise noted. Tubulin was purified from pig brain and labelled with tetramethylrhodamine (TMR) as described [66,67] and stored at -80°C after flash freezing in liquid N<sub>2</sub>. Partially TMR-labelled microtubules were polymerized from 1.7 µM 1.6:1 TMR-labelled tubulin and 33 µM unlabelled tubulin in the presence of 1 mM GTP, 4 mM MgCl<sub>2</sub> in BRB80 buffer, incubated for 20 min at 37°C. The microtubules were stabilized in BRB80 containing 10 µM paclitaxel (Taxol).

For cryo-EM experiments, microtubules were prepared from porcine brain tubulin (Cytoskeleton, Inc., CO). Tubulin lyophilized pellets were resuspended in BRB80 to 5 mg ml<sup>-1</sup> and spun at  $313\,000 \times g$  before polymerization to eliminate aggregates. Microtubule polymerization was done in conditions to enrich the number of microtubules with 15 protofilaments [68] as follows. The clarified resuspended tubulin solution was supplemented with 2 mM GTP, 4 mM MgCl<sub>2</sub>, 12% (v/v) DMSO and incubated 40 min at 37°C. An aliquot of stock paclitaxel (Taxol) solution (2 mM in DMSO) was added for a final paclitaxel concentration of  $250\,\mu\text{M}$  and incubated for another 40min at 37°C. The microtubules were then spun at  $15500 \times g$ , 25°C, and the pellet resuspended in BRB80 with 20 μM paclitaxel.

# 4.3. Determination of the KIF20A 55-510 NF structure by X-ray crystallography

#### 4.3.1. Crystallization

The 55-510 construct (20 mg ml<sup>-1</sup>) led to agglomerates of crystals in vapour diffusion setups at 17°C, in 2 M NaCl, 0.5 M (NH<sub>4</sub>)<sub>2</sub>SO<sub>4</sub>, 0.1 M Bis-Tris, pH 5.5, by mixing 1 µl of protein sample with an equal volume of precipitant. The initial crystals were optimized by seeding in 1.8 M NaCl, 0.5 M (NH<sub>4</sub>)<sub>2</sub>SO<sub>4</sub>, 0.1 M Bis-Tris, pH 5.5. Crystals were then harvested, cryo-protected with the above buffer supplemented with 20% glycerol and flash-frozen in liquid nitrogen for diffraction data collection.

#### 4.3.2. Diffraction data collection and processing, structure determination and refinement

Diffraction data were collected at the Proxima-1 beamline of the synchrotron SOLEIL (Saint-Aubin, France). Complete datasets were collected from individual crystals under a cryogenic stream at 100 K. All datasets were collected with a wavelength of 0.98 Å and processed using the automated pipeline autoPROC [69] that executes XDS [70], Pointless [71] and Aimless [72] of the CCP4 suite [73]. Se-SAD phasing was first performed using AutoSharp [69], with a crystal grown in presence of 2 mM Mg<sup>2+</sup>·ADP. No ADP was visible in the nucleotide binding site of the resulting model, which was thus refined against another native crystal dataset obtained in nucleotide-free conditions. This model was extended by iteratively using Buster [74] and Coot [75]. The refinement statistics of the final model (2.7 Å resolution) are shown in electronic supplementary material, table S1.

# 4.4. Determination of the KIF20A 1-565 NF structure in complex with microtubule by cryo-EM

#### 4.4.1. Sample preparation

Four microlitres of 6 µM microtubules BRB80 plus 20 µM paclitaxel were layered onto a (UltrAuFoil R1.2/1.3 300 mesh) plasma cleaned gold grid just before use (Gatan Solarus plasma cleaner, at 15 W for 6 s in a 75% argon/25% oxygen atmosphere), the microtubules were incubated 1 min at room temperature and then the excess liquid removed from the grid using a Whatman #1 paper. Four microlitres of the 40 µM KIF20A in BRB40 (40 mM PIPES, pH 6.8, 1 mM MgCl<sub>2</sub>, 1 mM EGTA) supplemented with 20 µM paclitaxel and  $20 \times 10^{-3}$  units of potato apyrase (Sigma-Aldrich, MO) were then applied onto the EM grid and incubated for 1 min at room temperature. The grid was mounted into a Vitrobot apparatus (FEI-ThermoFisher MA), incubated 1 min at room temperature and plunged frozen into liquid ethane. Vitrobot settings: 100% humidity, 3 s blotting with Whatman #1 paper and -2 mm offset. Grids were stored in liquid nitrogen until imaging in a cryo-electron microscope.

#### 4.4.2. Cryo-EM data collection

Data were collected at 300 kV on a Titan Krios microscope equipped with a K3 summit detector. Acquisition was controlled using Leginon [76] with the image-shift protocol (to target approximately 30 holes per stage shift) and partial correction for coma induced by beam tilt [77]. The pixel size was 0.844 Å pixel<sup>-1</sup> and the cumulated dose was 56 e<sup>-</sup>Å<sup>-2</sup> (electronic supplementary material, table S2). The exposures were fractionated on 40 movie frames.

#### 4.4.3. Processing of the cryo-EM datasets of microtubule—kinesin complexes

The processing was done as previously described [30]. Movie frames were aligned with Relion generating both dose-weighted and non-dose-weighted sums. Contrast transfer function (CTF) parameters per micrographs were estimated with Gctf [78] on aligned and non-dose-weighted movie averages.

Helical reconstruction on 15R microtubule was performed using a helical-single-particle 3D analysis workflow in Frealign [79], as described previously [30,80] with 664 pixels box size, with each filament contributing only to one of the two half datasets. Per-particle CTF refinement was performed with FrealignX [81].

To select for tubulins bound to kinesin motors and to improve the resolution of the kinesin-tubulin complexes, the procedure HSARC [30] was used for these one-head-bound states. The procedure follows these steps:

- (1) Relion helical refinement. The two independent Frealign helical refined half datasets were subjected to a single helical refinement in Relion 3.1 [82] where each dataset was assigned to a distinct half-set and using as priors the Euler angle values determined in the helical-singleparticle 3D reconstruction (initial resolution: 8 Å, sigma on Euler angles sigma\_ang: 1.5, no helical parameter
- (2) Asymmetric refinement with partial signal subtraction. An atomic model of a kinesin-tubulin complex was used to generate two soft masks using EMAN pdb2mrc and relion\_mask\_create (low-pass filtration: 30 Å, initial threshold: 0.05, extension: 14 pixels, soft edge: 8 pixels). One mask (mask<sub>full</sub>) was generated from a kinesin model bound to one tubulin dimer and two longitudinally flanking tubulin subunits while the other mask (mask<sub>kinesin</sub>) was generated with only the kinesin coordinates. The helical dataset alignment file was symmetry expanded using the 15R microtubule symmetry of the dataset. Partial signal subtraction was then performed using mask<sub>full</sub> to retain the signal within that mask. During this procedure, images were re-centred on the projections of 3D coordinates of the centre of mass of mask<sub>full</sub> (C<sub>M</sub>) using a 416 pixels box size. The partially signal subtracted dataset was then used in a Relion 3D refinement procedure using as priors the Euler angle values determined from the Relion helical refinement and the symmetry expansion procedure (initial resolution: 8 Å, sigma\_ang: 5, offset range corresponding to 5 Å, healpix order and auto local healpix order set to 5). The CTF of each particle was corrected to account for their different position along the optical axis.
- (3) 3D classification of the kinesin signal. A second partial signal subtraction procedure identical to the first one but using mask<sub>kinesin</sub> and with particles re-centred on the projections of  $C_{\rm M}$  was performed to subtract all but the kinesin signal. The images obtained were resampled to 3.5 Å pixel<sup>-1</sup> in 100-pixel boxes and the 3D refinement from step (2) was used to update the Euler angles and shifts of all particles. A 3D focused classification without image alignment and using a mask for the kinesin generated like  $mask_{kinesin}$  was then performed on the resampled dataset (8 classes, tau2 fudge: 4, padding: 2, iterations: 175). That classification led to one class with a kinesin visible (12.8% of the dataset). As the decoration was low and the kinesin density heterogeneous, another round of 3D classification in 8 classes with the same parameters was performed on the subset of data corresponding to that decorated class. This generated 2 classes with a kinesin having some secondary structure visible, the rest being at

too low a resolution on the kinesin part for proper assessment. So, the decorated subset of the data (12.8% of the dataset) was used as input in a 3D classification with only 2 classes. The final 2 classes, class-1 and class-2, comprised 66% and 33% of the input data respectively (8.6% and 4.2% of the dataset).

(4) 3D reconstructions with original images (not signal subtracted). To avoid potential artefacts introduced by the signal subtraction procedure, final 3D reconstructions were obtained using relion\_reconstruct on the original image-particles without signal subtraction.

To obtain a final locally filtered and locally sharpened map for the higher resolution class-1, post-processing of the pair of unfiltered and unsharpened half maps was performed as follows. One of the two unfiltered half-maps was low-passfiltered to 15 Å and the minimal threshold value that does not show noise around the microtubule fragment was used to generate a mask with relion\_mask\_create (low-pass filtration: 15 Å, extension: 10 pixels, soft edge: 10 pixels). This soft mask was used in blocres [83] on 12-pixel size boxes to obtain initial local resolution estimates. The merged map was locally filtered by blocfilt [83] using blocres local resolution estimates and then used for local low-pass filtration and local sharpening in localdeblur [84] with resolution search up to 25 Å. The localdeblur program converged to a filtration appropriate for the tubulin part of the map but over-sharpened for the kinesin part. The maps at every localdeblur cycle were saved and the map with better filtration for the kinesin part area was selected with the aim of better resolving the kinesin loops. For the lower resolution class-2, the map was postprocessed in Relion, applying a bfactor of  $-80 \text{ Å}^2$  and low pass filtered at 4 Å.

#### 4.4.4. Cryo-EM resolution estimation

The final resolutions for each cryo-EM class average reconstruction were estimated from FSC curves generated with Relion 3.1 postprocess (FSC<sub>0.143</sub> criteria; electronic supplementary material, figure S4). To estimate the overall resolution, these curves were computed from the two independently refined half maps (gold standard) using soft masks that isolate a single asymmetric unit containing a kinesin and a tubulin dimer. The soft masks were created with Relion 3.1 relion\_mask\_create (for microtubule datasets: low pass filtration: 15 Å, threshold: 0.1, extension: 2 pixels, soft edge: 5 pixels) applied on the correctly positioned EMAN pdb2mrc density map generated with the coordinates of the respective refined atomic models. FSC curves for the tubulin or kinesin parts of the maps were generated similarly using the corresponding subset of the PDB model to mask only a kinesin or a tubulin dimer (electronic supplementary material, table S2).

## 4.5. Steady state ATPase assays and pre-steady state kinetics

ATPase assays were performed using the EnzChek phosphate assay kit (Invitrogen) with motor concentrations in the 5 to 50 nM range and 25 nM to 20 µM polymerized tubulin. ATPase assays were performed in 25 mM HEPES, 50 mM potassium acetate, 5 mM magnesium acetate, 1 mM EGTA, and 1 mM DTT, pH 7.5.  $k_{\rm cat}$  and  $K_{0.5,\rm MT}$  were calculated from fitting the Michaelis-Menten equation to ATPase data taken at a >10-fold excess of microtubules.

Pre-steady-state kinetics of 2' deoxy 3' MANT-ATP (2'dmT) binding, nucleotide-dependent microtubule release and Pi release were performed on a KinTex SF-2004 stopped-flow apparatus as previously described [85].

Binding of the fluorescent nucleotide analogue 2'dmT to 4:1 microtubules:motor complex was measured by mixing with an excess of fluorescent nucleotide in a KinTek F-300X stopped flow at 20°C, with instrument dead time of 1.2 ms. Samples were rendered nucleotide-free prior to mixing by incubating for 20 min with 0.2 U ml<sup>-1</sup> apyrase (Type VII, Sigma Aldrich, St Louis, MO). Fluorescence enhancement of the MANT-fluorophore was monitored by energy transfer from vicinal tryptophans by exciting at 295 nm and monitoring 90° from the incident beam through a 450 nm broad bandpass filter (Omega Optical, Brattleboro, VT). Data were subjected to linear least squares fitting.

### 4.6. Gliding motility assays

Gliding motility assays were performed as described previously [63] at room temperature (23°C) or at 30°C. 0.5–1.0 µM motor solutions were filled into assay chambers (KIF20A constructs, Kin-1 and Kin-3) and were allowed to specifically bind to the coverslips of the assay chambers pre-treated with protein G and an Anti-His antibody. Chambers were made from 22 mm × 24 mm cleaned coverslips spaced from 75 mm × 25 mm cleaned microscope slides (electronic supplementary material, figure S11) using double-sided tape of approximately 100 µm thickness (Tesa SE, Hamburg, Germany). After motor attachment, chambers were filled with 10 µl TMR-labelled microtubules (approx. 0.4 µM tubulin dimers in anti-bleach buffer containing 2 mM ATP). Anti-bleach buffer contained 80 μg ml<sup>-1</sup> catalase, 100 μg ml<sup>-1</sup> glucose oxidase, 10 mM D-glucose and 10 µM paclitaxel, in BRB80 buffer.

Motility was observed in an inverted fluorescence microscope (Axiovert 200, Carl Zeiss, Jena, Germany) using a Zeiss EC Plan-Neofluar 100× 1.3 NA oil immersion objective. Images were recorded with a CCD camera (Photometrics Cool-Snap EZ; Roper Scientific GmbH, Ottobrunn, Germany). Data were acquired with WinSpec software (Princeton Instruments, Princeton, NJ, USA). Further analysis and statistical calculations were performed with MATLAB (The MathWorks, Natick, MA, USA) and Fiji/ImageJ (NIH).

#### 4.7. Single-molecule motility assays

Coverslips were cleaned using 0.5 mM KOH prior to silanization with a positively charged silane, 3-[2-(2-aminoethylamino)ethylamino]propyltrimethoxysilane (Sigma-Aldrich, Hamburg, Germany) for microtubule immobilization. Microtubules were incubated on the treated coverslips for 10 min followed by 10 min incubation with 0.1 mg ml<sup>-1</sup> casein (Sigma-Aldrich) in BRB80 buffer. The chamber was then washed with 10 µl of assay buffer (BRB80 buffer + anti-bleaching agents) and then filled with 10 µl of 20-50 nM of GFP-tagged motor proteins (KIF20A 1-665 and Kin-5) in assay buffer containing 2 mM ATP. Fluorescence was observed in a custom-built total internal reflection fluorescence (TIRF) microscope described previously [86] using an oilimmersion objective (SFluor 100×, NA 1.49, Nikon Instruments Europe BV, Amsterdam, Netherlands). Images were recorded

with a CCD camera (Ixon Ultra, Andor Technology, Oxford Instruments, Oxford, UK). Videos were recorded at 10 frames per second and were analysed for motor speeds using kymographs generated with Solis software from Andor. Statistical analysis of the data was performed with MATLAB (The Math-Works) and Fiji/ImageJ (NIH). All experiments were performed at room temperature (23°C).

The dwell times of GFP-tagged motor proteins in the regions selected for kymographs were measured from the kymographs that were generated from unprocessed image sequences using ImageJ. Start and end points of individual dwell events were determined from kymograph intensity profiles (figure 5b,c) using a threshold of 10% of the maximal intensity. Note that brief appearances of fluorescent proteins can also occur due to diffusion in and out of the TIRF detection zone of about 200 nm depth near the substrate surface.

#### 4.8. Small angle X-ray scattering

SAXS data were collected on the SWING beamline (synchrotron SOLEIL, Saint-Aubin, France). Purified KIF20A 1-565 was incubated with ADP for 15 min on ice, and then all samples were centrifuged at 20 000 x g for 10 min at 4°C prior to the analysis. 45  $\mu$ l of the protein at 4.43 mg mL<sup>-1</sup> (70.4 µM) was injected in SEC column S200i 5/150 (GE Life Sciences, Velizy-Villacoublay, France) with a buffer containing 20 mM HEPES, pH 7.5, 1 mM DTT, 150 mM NaCl, 5 mM MgCl<sub>2</sub> and supplemented with 5 mM of nucleotide when appropriate. All datasets were processed using Foxtrot software (version 3.5.9) (Xenocs Soleil Synchrotron, Sassenage, France) [87], then Rg value calculations were performed using Primus software [88].

Ethics. This work did not require ethical approval from a human subject or animal welfare committee.

Data accessibility. The atomic models are available in the PDB, www. pdb.org, under accession numbers PDB 8BJS for the KIF20A-MD-NF X-ray structure (electronic supplementary material, table S1), and 8F1A and 8F18 for the cryo-EM structure (class-1 and class-2, respectively). The final cryo-EM maps together with the corresponding half maps, masks used for resolution estimation, masks used in the partial signal subtraction for the microtubule datasets, and the FSC curves are deposited in the Electron Microscopy Data Bank, under accession numbers EMD-28789 and EMD-28787 (electronic supplementary material, table S2).

PDB: 8BJS 10.2210/pdb8bjs PDB: 8F1A 10.2210/pdb8f1a PDB: 8F18 10.2210/pdb8f18

The data are provided in electronic supplementary material [89]. Declaration of Al use. We have not used AI-assisted technologies in creating this article.

Authors' contributions. F.M.R.: formal analysis, investigation, methodology, supervision, validation, writing-original draft, writingreview and editing; V.C.: formal analysis, investigation, methodology, validation, writing-original draft, writing-review and editing; M.P.M.H.B.: formal analysis, investigation, methodology, validation, writing-original draft, writing-review and editing; A.A.M.K.: data curation, investigation, methodology, writing-original draft, writing-and editing; C.K.: investigation, methodology, writingreview and editing; H.S.: investigation, methodology, writingreview and editing; A.E.M.: methodology, writing—review and editing; S.M.-L.: investigation, validation, writing—review and editing; A.B.A.: investigation, methodology; H.S.: formal analysis, funding acquisition, investigation, methodology, supervision, validation, writing-original draft, writing-review and editing; C.F.S.: data curation, formal analysis, funding acquisition, investigation, methodology, project administration, supervision, validation, writingoriginal draft, writing—review and editing; S.S.R.: conceptualization, formal analysis, funding acquisition, investigation, methodology, project administration, supervision, validation, writing-original draft, writing-review and editing; A.H.: conceptualization, data curation, formal analysis, funding acquisition, investigation, methodology, project administration, supervision, validation, visualization, writing—original draft, writing—review and editing.

All authors gave final approval for publication and agreed to be held accountable for the work performed therein.

Conflict of interest declaration. We declare we have no competing interests. Funding. We thank Biokinesis, Inc. for financial support of one-year post-doctoral fellow. This work was further supported by NIH NS073610-01, GM113164 (H.S.); GM130556, U54CA210190 to S.S.R., the European Research Council under the European Union's Seventh Framework Programme (FP7/2007–2013)/ERC grant agreement no. 340528 to C.F.S.; ANR/DFG project: ANR-15-CE13-0017-01 and DFG-AZ:SCHM 799/6-1 to A.H. and C.F.S. Cryo-EM data collection was performed at the Simons Electron Microscopy Center and National Resource for Automated Molecular Microscopy located at the New York Structural Biology Center, supported by grants from the Simons Foundation (SF349247), NYSTAR, and the NIH National Institute of General Medical Sciences (GM103310) with additional support from Agouron Institute (F00316) and NIH (OD019994). A.H. was supported by an IRP grant from CNRS, la Ligue contre le Cancer Comité de Paris RS20/75-D, ARC 2016-1-PLBIO-10-ICR-1, FRM DCM20181039553 and INCA 2016-1-PLBIO-10-ICR-1. The AH team is part of the Labex Cell(n)Scale (ANR-11-LABX-0038), which is part of the IsDEX PSL (ANR-10-IDEX-0001-02).

Acknowledgements. We thank I-Mei Yu for preliminary experiments performed for this project. We are grateful to the beamline scientists of PX1 (SOLEIL synchrotron) for excellent support and we thank Margaret A. Titus and members of the Structural Motility group together with Bruno Goud and Phong Thanh Tran for critical reading of the manuscript.

## References

- 1. Kozielski F. 2015 Kinesins and cancer. Dordrecht, The Netherlands: Springer Netherlands.
- Hill E, Clarke M, Barr FA. 2000 The Rab6-binding kinesin, Rab6-KIFL, is required for cytokinesis. EMBO J. **19**, 5711–5719. (doi:10.1093/emboj/19.21.5711)
- Fontijn RD, Goud B, Echard A, Jollivet F, van Marle J, Pannekoek H, Horrevoets AJG. 2001 The human kinesin-like protein RB6K is under tight cell cycle control and is essential for cytokinesis. Mol. Cell. Biol. 21, 2944-2955. (doi:10.1128/MCB.21.8.2944-2955.2001)
- Echard A, Jollivet F, Martinez O, Lacapère J-J, Rousselet A, Janoueix-Lerosey I, Goud B. 1998

- Interaction of a Golgi-associated kinesin-like protein with Rab6. Science 279, 580-585. (doi:10.1126/ science.279.5350.580)
- Echard A, el Marjou A, Goud B. 2001 Expression, purification, and biochemical properties of rabkinesin-6 domains and their interactions with Rab6A. Methods Enzymol. **329**, 157–165. (doi:10.1016/s0076-6879(01) 29076-4)
- Miserey-Lenkei S et al. 2017 Coupling fission and exit of RAB6 vesicles at Golgi hotspots through kinesin-myosin interactions. Nat. Commun. 8, 1254. (doi:10.1038/s41467-017-01266-0)
- Landino J, Norris SR, Li M, Ballister ER, Lampson MA, Ohi R. 2017 Two mechanisms coordinate the recruitment of the chromosomal passenger complex to the plane of cell division. Mol. Biol. Cell 28, 3634-3646. (doi:10.1091/mbc.
- Gruneberg U, Neef R, Honda R, Nigg EA, Barr FA. 2004 Relocation of Aurora B from centromeres to the central spindle at the metaphase to anaphase transition requires MKlp2. J. Cell Biol. 166, 167-172. (doi:10.1083/jcb.200403084)
- Gasnereau I et al. 2012 KIF20A mRNA and its product MKlp2 are increased during hepatocyte proliferation

- and hepatocarcinogenesis. Am. J. Pathol. 180, 131-140. (doi:10.1016/j.ajpath.2011.09.040)
- 10. Saito K, Ohta S, Kawakami Y, Yoshida K, Toda M. 2017 Functional analysis of KIF20A, a potential immunotherapeutic target for glioma. J. Neurooncol. **132**, 63-74. (doi:10.1007/s11060-016-2360-1)
- 11. Taniuchi K, Nakagawa H, Nakamura T, Eguchi H, Ohigashi H, Ishikawa O, Katagiri T, Nakamura Y. 2005 Down-regulation of RAB6KIFL/KIF20A, a kinesin involved with membrane trafficking of discs large homologue 5, can attenuate growth of pancreatic cancer cell. Cancer Res. 65, 105-112. (doi:10.1158/0008-5472.105.65.1)
- 12. Yan G-R, Zou F-Y, Dang B-L, Zhang Y, Yu G, Liu X, He Q-Y. 2012 Genistein-induced mitotic arrest of gastric cancer cells by downregulating KIF20A, a proteomics study. Proteomics 12, 2391-2399. (doi:10.1002/pmic.201100652)
- 13. Zhang Z, Chai C, Shen T, Li X, Ji J, Li C, Shang Z, Niu Y. 2019 Aberrant KIF20A expression is associated with adverse clinical outcome and promotes tumor progression in prostate cancer. Dis. Markers 2019, e4782730. (doi:10.1155/2019/4782730)
- 14. Copello VA, Burnstein KL. 2022 The kinesin KIF20A promotes progression to castration-resistant prostate cancer through autocrine activation of the androgen receptor. Oncogene 41, 2824-2832. (doi:10.1038/ s41388-022-02307-9)
- 15. Tcherniuk S, Skoufias DA, Labriere C, Rath O, Gueritte F, Guillou C, Kozielski F. 2010 Relocation of Aurora B and survivin from centromeres to the central spindle impaired by a kinesin-specific MKLP-2 inhibitor. Angew. Chem. Int. Ed. Engl. 49, 8228-8231. (doi:10.1002/anie.201003254)
- 16. Ferrero H, Corachán A, Quiñonero A, Bougeret C, Pouletty P, Pellicer A, Domínguez F. 2019 Inhibition of KIF20A by BKS0349 reduces endometriotic lesions in a xenograft mouse model. Mol. Hum. Reprod. 25, 562-571. (doi:10.1093/molehr/gaz044)
- 17. Hümmer S, Mayer TU. 2009 Cdk1 negatively regulates midzone localization of the mitotic kinesin Mklp2 and the chromosomal passenger complex. Curr. Biol. 19, 607-612. (doi:10.1016/j.cub.2009.02.
- 18. Kitagawa M, Fung SYS, Hameed UFS, Goto H, Inagaki M, Lee SH. 2014 Cdk1 coordinates timely activation of MKlp2 kinesin with relocation of the chromosome passenger complex for cytokinesis. Cell Rep. 7, 166-179. (doi:10.1016/j. celrep.2014.02.034)
- 19. Fung SYS, Kitagawa M, Liao P-J, Wong J, Lee SH. 2017 Opposing activities of Aurora B kinase and B56-PP2A phosphatase on MKlp2 determine abscission timing. Curr. Biol. 27, 78-86. (doi:10. 1016/j.cub.2016.10.042)
- 20. Neef R, Preisinger C, Sutcliffe J, Kopajtich R, Nigg EA, Mayer TU, Barr FA. 2003 Phosphorylation of mitotic kinesin-like protein 2 by polo-like kinase 1 is required for cytokinesis. J. Cell Biol. 162, 863-876. (doi:10.1083/jcb.200306009)
- 21. Pavicic-Kaltenbrunner V, Mishima M, Glotzer M. 2007 Cooperative assembly of CYK-4/MgcRacGAP and ZEN-4/MKLP1 to form the centralspindlin

- complex. Mol. Biol. Cell 18, 4992-5003. (doi:10. 1091/mbc.e07-05-0468)
- 22. Mishima M, Kaitna S, Glotzer M. 2002 Central spindle assembly and cytokinesis require a kinesinlike protein/RhoGAP complex with microtubule bundling activity. Dev. Cell 2, 41-54. (doi:10.1016/ \$1534-5807(01)00110-1)
- 23. Janisch KM, McNeely KC, Dardick JM, Lim SH, Dwyer ND. 2018 Kinesin-6 KIF20B is required for efficient cytokinetic furrowing and timely abscission in human cells. Mol. Biol. Cell 29, 166-179. (doi:10. 1091/mbc.E17-08-0495)
- 24. Poulos A, Budaitis BG, Verhey KJ. 2022 Single-motor and multi-motor motility properties of kinesin-6 family members. Biol. Open 11, bio059533. (doi:10. 1242/bio.059533)
- 25. Atherton J et al. 2017 The divergent mitotic kinesin MKLP2 exhibits atypical structure and mechanochemistry. Elife 6, e27793. (doi:10.7554/ eLife.27793)
- 26. Andreasson JO, Milic B, Chen G-Y, Guydosh NR, Hancock WO, Block SM. 2015 Examining kinesin processivity within a general gating framework. Elife **4**, e07403. (doi:10.7554/eLife.07403)
- 27. Yildiz A, Tomishige M, Gennerich A, Vale RD. 2008 Intramolecular strain coordinates kinesin stepping behavior along microtubules. Cell 134, 1030-1041. (doi:10.1016/j.cell.2008.07.018)
- 28. Adriaans IE, Hooikaas PJ, Aher A, Vromans MJM, van Es RM, Grigoriev I, Akhmanova A, Lens SMA. 2020 MKLP2 Is a motile kinesin that transports the chromosomal passenger complex during anaphase. Curr. Biol. 30, 2628-2637. (doi:10.1016/j.cub.2020. 04.081)
- 29. Guan R, Zhang L, Su QP, Mickolajczyk KJ, Chen G-Y, Hancock WO, Sun Y, Zhao Y, Chen Z. 2017 Crystal structure of Zen4 in the apo state reveals a missing conformation of kinesin. Nat. Commun. 8, 14951. (doi:10.1038/ncomms14951)
- 30. Benoit MPMH, Asenjo AB, Paydar M, Dhakal S, Kwok BH, Sosa H. 2021 Structural basis of mechano-chemical coupling by the mitotic kinesin KIF14. Nat. Commun. 12, 3637. (doi:10.1038/ s41467-021-23581-3)
- 31. Kull FJ, Sablin EP, Lau R, Fletterick RJ, Vale RD. 1996 Crystal structure of the kinesin motor domain reveals a structural similarity to myosin. Nature 380, 550-555. (doi:10.1038/380550a0)
- 32. Cao L, Wang W, Jiang Q, Wang C, Knossow M, Gigant B. 2014 The structure of apo-kinesin bound to tubulin links the nucleotide cycle to movement. *Nat. Commun.* **5**, 5364. (doi:10.1038/ncomms6364)
- 33. Shang Z, Zhou K, Xu C, Csencsits R, Cochran JC, Sindelar CV. 2014 High-resolution structures of kinesin on microtubules provide a basis for nucleotide-gated force-generation. eLife 3, e04686. (doi:10.7554/eLife.04686)
- Parke CL, Wojcik EJ, Kim S, Worthylake DK. 2010 ATP Hydrolysis in Eq5 kinesin involves a catalytic two-water mechanism. J. Biol. Chem. 285, 5859-5867. (doi:10.1074/jbc.M109.071233)
- 35. Gigant B, Wang W, Dreier B, Jiang Q, Pecqueur L, Plückthun A, Wang C, Knossow M. 2013 Structure of

- a kinesin-tubulin complex and implications for kinesin motility. Nat. Struct. Mol. Biol. 20, 1001-1007. (doi:10.1038/nsmb.2624)
- 36. Hunter B, Benoit MPMH, Asenjo AB, Doubleday C, Trofimova D, Frazer C, Shoukat I, Sosa H, Allingham JS. 2022 Kinesin-8-specific loop-2 controls the dual activities of the motor domain according to tubulin protofilament shape. Nat. Commun. 13, 4198. (doi:10.1038/s41467-022-31794-3)
- 37. Cao L, Cantos-Fernandes S, Gigant B. 2017 The structural switch of nucleotide-free kinesin. Sci. Rep. 7, 42558. (doi:10.1038/srep42558)
- 38. Arora K, Talje L, Asenjo AB, Andersen P, Atchia K, Joshi M, Sosa H, Allingham JS, Kwok BH. 2014 KIF14 binds tightly to microtubules and adopts a rigor-like conformation. J. Mol. Biol. 426, 2997-3015. (doi:10.1016/j.jmb.2014.05.030)
- 39. Hwang W, Lang MJ, Karplus M. 2017 Kinesin motility is driven by subdomain dynamics. Elife 6, e28948. (doi:10.7554/eLife.28948)
- 40. Chang Q, Nitta R, Inoue S, Hirokawa N. 2013 Structural basis for the ATP-induced isomerization of kinesin. J. Mol. Biol. 425, 1869-1880. (doi:10.1016/ j.jmb.2013.03.004)
- 41. Düselder A, Thiede C, Schmidt CF, Lakämper S. 2012 Neck-linker length dependence of processive Kinesin-5 motility. J. Mol. Biol. 423, 159-168. (doi:10.1016/j.jmb.2012.06.043)
- Kaneko T, Furuta K, Oiwa K, Shintaku H, Kotera H, Yokokawa R. 2020 Different motilities of microtubules driven by kinesin-1 and kinesin-14 motors patterned on nanopillars. Sci. Adv. 6, eaax7413. (doi:10.1126/sciadv.aax7413)
- Rosenfeld SS, Taylor EW. 1984 Reactions of 1-N6-ethenoadenosine nucleotides with myosin subfragment 1 and acto-subfragment 1 of skeletal and smooth muscle. J. Biol. Chem. 259, 11 920-11 929. (doi:10.1016/S0021-9258(20)71299-8)
- 44. Cochran JC, Sontag CA, Maliga Z, Kapoor TM, Correia JJ, Gilbert SP. 2004 Mechanistic analysis of the mitotic kinesin Eg5. J. Biol. Chem. 279, 38 861-38 870. (doi:10.1074/jbc.M404203200)
- 45. Pettersen EF, Goddard TD, Huang CC, Couch GS, Greenblatt DM, Meng EC, Ferrin TE. 2004 UCSF Chimera—a visualization system for exploratory research and analysis. J. Comput. Chem. 25, 1605-1612. (doi:10.1002/jcc.20084)
- 46. Nitta R, Okada Y, Hirokawa N. 2008 Structural model for strain-dependent microtubule activation of Mg-ADP release from kinesin. Nat. Struct. Mol. *Biol.* **15**, 1067–1075. (doi:10.1038/nsmb.1487)
- 47. Ren J, Zhang Y, Wang S, Huo L, Lou J, Feng W. 2018 Structural delineation of the neck linker of kinesin-3 for processive movement. J. Mol. Biol. **430**, 2030–2041. (doi:10.1016/j.jmb.2018.05.010)
- Sindelar CV. 2011 A seesaw model for intermolecular gating in the kinesin motor protein. Biophys. Rev. 3, 85. (doi:10.1007/s12551-011-0049-4)
- 49. Budaitis BG, Jariwala S, Reinemann DN, Schimert KI, Scarabelli G, Grant BJ, Sept D, Lang MJ, Verhey KJ. 2019 Neck linker docking is critical for Kinesin-1 force generation in cells but at a cost to motor speed and processivity. eLife 8, e44146. (doi:10.7554/eLife.44146)

- 50. Clancy BE, Behnke-Parks WM, Andreasson JOL, Rosenfeld SS, Block SM. 2011 A universal pathway for kinesin stepping. Nat. Struct. Mol. Biol. 18, 1020-1027. (doi:10.1038/nsmb.2104)
- 51. Hackney DD, Stock MF, Moore J, Patterson RA. 2003 Modulation of kinesin half-site ADP release and kinetic processivity by a spacer between the head groups. Biochemistry 42, 12 011-12 018. (doi:10. 1021/bi0349118)
- 52. Shastry S, Hancock WO. 2010 Neck linker length determines the degree of processivity in kinesin-1 and kinesin-2 motors. Curr. Biol. 20, 939-943. (doi:10.1016/j.cub.2010.03.065)
- 53. Hwang W, Lang MJ, Karplus M. 2008 Force generation in kinesin hinges on cover-neck bundle formation. Structure 16, 62-71. (doi:10.1016/j.str. 2007.11.008)
- 54. Khalil AS, Appleyard DC, Labno AK, Georges A, Karplus M, Belcher AM, Hwang W, Lang MJ. 2008 Kinesin's cover-neck bundle folds forward to generate force. Proc. Natl Acad. Sci. USA 105, 19 247-19 252. (doi:10.1073/pnas.0805147105)
- 55. Miller BM, Bloemink MJ, Nyitrai M, Bernstein SI, Geeves MA. 2007 A variable domain near the ATP binding site in Drosophila muscle myosin is part of the communication pathway between the nucleotide and actin-binding sites. J. Mol. Biol. 368, 1051-1066. (doi:10.1016/j.jmb.2007.02.042)
- 56. Moyer ML, Gilbert SP, Johnson KA. 1998 Pathway of ATP hydrolysis by monomeric and dimeric kinesin. Biochemistry 37, 800-813. (doi:10.1021/bi9711184)
- 57. Rosenfeld SS, Xing J, Jefferson GM, King PH. 2005 Docking and rolling, a model of how the mitotic motor Eg5 works. J. Biol. Chem. 280, 35 684-35 695. (doi:10.1074/jbc.M506561200)
- Mickolajczyk KJ, Cook ASI, Jevtha JP, Fricks J, Hancock WO. 2019 Insights into kinesin-1 stepping from simulations and tracking of gold nanoparticlelabeled motors. Biophys. J. 117, 331-345. (doi:10. 1016/j.bpj.2019.06.010)
- 59. Goulet A, Major J, Jun Y, Gross SP, Rosenfeld SS, Moores CA. 2014 Comprehensive structural model of the mechanochemical cycle of a mitotic motor highlights molecular adaptations in the kinesin family. Proc. Natl Acad. Sci. USA 111, 1837-1842. (doi:10.1073/pnas.1319848111)
- 60. Rice S et al. 1999 A structural change in the kinesin motor protein that drives motility. Nature 402, 778-784. (doi:10.1038/45483)
- 61. Sablin EP, Fletterick RJ. 2004 Coordination between motor domains in processive kinesins. J. Biol. Chem. **279**, 15 707-15 710. (doi:10.1074/ jbc.R300036200)
- 62. Turner J, Anderson R, Guo J, Beraud C, Fletterick R, Sakowicz R. 2001 Crystal structure of the mitotic spindle kinesin Eg5 reveals a novel conformation of the neck-linker. J. Biol. Chem. 276, 25 496-25 502. (doi:10.1074/jbc.M100395200)

- 63. Lakämper S, Thiede C, Düselder A, Reiter S, Korneev MJ, Kapitein LC, Peterman EJG, Schmidt CF. 2010 The effect of monastrol on the processive motility of a dimeric kinesin-5 head/kinesin-1 stalk chimera. *J. Mol. Biol.* **399**, 1–8. (doi:10.1016/j.jmb.2010.03.
- 64. Klopfenstein DR, Tomishige M, Stuurman N, Vale RD. 2002 Role of phosphatidylinositol(4,5)bisphosphate organization in membrane transport by the Unc104 kinesin motor. Cell 109, 347-358. (doi:10.1016/S0092-8674(02)00708-0)
- 65. Tomishige M, Klopfenstein DR, Vale RD. 2002 Conversion of Unc104/KIF1A kinesin into a processive motor after dimerization. Science 297, 2263-2267. (doi:10.1126/science.1073386)
- 66. Hyman A, Drechsel D, Kellogg D, Salser S, Sawin K, Steffen P, Wordeman L, Mitchison T. 1991 Preparation of modified tubulins. Methods Enzymol. 196, 478-485. (doi:10.1016/0076-6879(91)96041-
- 67. Williams RC, Lee JC. 1982 Preparation of tubulin from brain. Methods Enzymol. 85, 376-385. (doi:10. 1016/0076-6879(82)85038-6)
- 68. Wilson-Kubalek EM, Cheeseman IM, Milligan RA. 2016 Structural comparison of the Caenorhabditis elegans and human Ndc80 complexes bound to microtubules reveals distinct binding behavior. Mol. Biol. Cell 27, 1197-1203. (doi:10.1091/mbc.E15-12-
- 69. Vonrhein C, Flensburg C, Keller P, Sharff A, Smart O, Paciorek W, Womack T, Bricogne G. 2011 Data processing and analysis with the autoPROC toolbox. Acta Crystallogr. D Biol. Crystallogr. 67, 293-302. (doi:10.1107/S0907444911007773)
- Kabsch W. 2010 XDS. Acta Crystallogr. D Biol. Crystallogr. 66, 125-132. (doi:10.1107/ S0907444909047337)
- 71. Evans P. 2006 Scaling and assessment of data quality. Acta Crystallogr. D Biol. Crystallogr. 62, 72-82. (doi:10.1107/S0907444905036693)
- 72. Evans PR, Murshudov GN. 2013 How good are my data and what is the resolution? Acta Crystallogr. D Biol. Crystallogr. 69, 1204-1214. (doi:10.1107/ S0907444913000061)
- 73. Winn MD et al. 2011 Overview of the CCP4 suite and current developments. Acta Crystallogr. D Biol. Crystallogr. 67, 235-242. (doi:10.1107/ S0907444910045749)
- 74. Bricogne G et al. 2017 BUSTER version 2.10.3. Cambridge, UK: Global Phasing Ltd.
- 75. Emsley P, Lohkamp B, Scott WG, Cowtan K. 2010 Features and development of Coot. Acta Crystallogr. D Biol. Crystallogr. 66, 486-501. (doi:10.1107/ S0907444910007493)
- 76. Suloway C, Pulokas J, Fellmann D, Cheng A, Guerra F, Quispe J, Stagg S, Potter CS, Carragher B. 2005 Automated molecular microscopy: the new Leginon

- system. J. Struct. Biol. 151, 41-60. (doi:10.1016/j. jsb.2005.03.010)
- 77. Glaeser RM, Typke D, Tiemeijer PC, Pulokas J, Cheng A. 2011 Precise beam-tilt alignment and collimation are required to minimize the phase error associated with coma in high-resolution cryo-EM. J. Struct. *Biol.* **174**, 1–10. (doi:10.1016/j.jsb.2010.12.005)
- 78. Zhang K. 2016 Gctf: real-time CTF determination and correction. J. Struct. Biol. 193, 1-12. (doi:10. 1016/j.jsb.2015.11.003)
- 79. Grigorieff N. 2016 Frealign: an exploratory tool for single-particle Cryo-EM. Methods Enzymol. 579, 191-226. (doi:10.1016/bs.mie. 2016.04.013)
- 80. Benoit MPMH, Asenjo AB, Sosa H. 2018 Cryo-EM reveals the structural basis of microtubule depolymerization by kinesin-13s. Nat. Commun. 9, 1662. (doi:10.1038/s41467-018-04044-8)
- 81. Grant T, Rohou A, Grigorieff N. 2018 cisTEM, userfriendly software for single-particle image processing. Elife 7, e35383. (doi:10.7554/eLife. 35383)
- 82. Zivanov J, Nakane T, Forsberg BO, Kimanius D, Hagen WJ, Lindahl E, Scheres SH. 2018 New tools for automated high-resolution cryo-EM structure determination in RELION-3. Elife 7, e42166. (doi:10. 7554/eLife.42166)
- 83. Heymann JB, Belnap DM. 2007 Bsoft: image processing and molecular modeling for electron microscopy. J. Struct. Biol. 157, 3-18. (doi:10.1016/ j.jsb.2006.06.006)
- 84. Ramírez-Aportela E et al. 2020 Automatic local resolution-based sharpening of cryo-EM maps. Bioinformatics 36, 765-772. (doi:10.1093/ bioinformatics/btz671)
- 85. Muretta JM, Behnke-Parks WM, Major J, Petersen KJ, Goulet A, Moores CA, Thomas DD, Rosenfeld SS. 2013 Loop L5 assumes three distinct orientations during the ATPase cycle of the mitotic kinesin Eg5. J. Biol. Chem. 288, 34 839-34 849. (doi:10.1074/ jbc.M113.518845)
- 86. Fish KN. 2009 Total internal reflection fluorescence (TIRF) microscopy. Curr. Protoc. Cytom. 50, 12-18. (doi:10.1002/0471142956.cy1218s50)
- 87. Tencé-Girault S, Lebreton S, Bunau O, Dang P, Bargain F. 2019 Simultaneous SAXS-WAXS experiments on semi-crystalline polymers: example of PA11 and its brill transition. Crystals 9, 1-17. (doi:10.3390/cryst9050271)
- Konarev PV, Volkov VV, Sokolova AV, Koch MHJ, Svergun DI. 2003 PRIMUS: a Windows PC-based system for small-angle scattering data analysis. J. Appl. Crystallogr. 36, 1277-1282. (doi:10.1107/ 50021889803012779)
- 89. Ranaivoson FM et al. 2023 Nucleotide-free structures of KIF20A illuminate atypical mechanochemistry in this kinesin-6. Figshare. (doi:10.6084/m9.figshare.c.6821440)